JGR Space Physics

RESEARCH ARTICLE
10.1029/2025JA034327

Reassessing the Relationship Between Meteor Radio Afterglows and Optical Persistent Trains

L. E. Cordonnier[1,2], K. S. Obenberger[1], G. B. Taylor[2], J. M. Holmes[1], J. Dowell[2], and D. Vida[3]

[1]Space Vehicles Directorate, Air Force Research Laboratory, Kirtland AFB, NM, USA, [2]Department of Physics and Astronomy, University of New Mexico, Albuquerque, NM, USA, [3]Department of Physics and Astronomy, University of Western Ontario, London, ON, Canada

Key Points:

- Meteor radio afterglows (MRAs) and persistent trains (PTs) are not strongly related to one another and often form independently
- MRA occurrence rates do not undergo strong variations throughout the year, in contrast to PTs
- The MRA occurrence rate shows a strong observational dependence on meteor entry angle, with MRAs favoring shallower trajectories

Correspondence to:
L. E. Cordonnier,
lcordonnier@unm.edu

Citation:
Cordonnier, L. E., Obenberger, K. S., Taylor, G. B., Holmes, J. M., Dowell, J., & Vida, D. (2025). Reassessing the relationship between meteor radio afterglows and optical persistent trains. *Journal of Geophysical Research: Space Physics*, *130*, e2025JA034327. https://doi.org/10.1029/2025JA034327

Received 16 JUN 2025
Accepted 12 AUG 2025

Author Contributions:
Conceptualization: L. E. Cordonnier, K. S. Obenberger, G. B. Taylor, J. M. Holmes, J. Dowell
Data curation: L. E. Cordonnier, G. B. Taylor, J. Dowell, D. Vida
Formal analysis: L. E. Cordonnier
Funding acquisition: K. S. Obenberger, G. B. Taylor, J. M. Holmes
Investigation: L. E. Cordonnier, K. S. Obenberger
Methodology: L. E. Cordonnier, K. S. Obenberger, J. Dowell, D. Vida
Project administration: K. S. Obenberger, G. B. Taylor, J. M. Holmes
Resources: L. E. Cordonnier, K. S. Obenberger, G. B. Taylor, J. M. Holmes, J. Dowell, D. Vida

Abstract Meteor radio afterglows (MRAs) and optical persistent trains (PTs) are two types of long-lived phenomena which are occasionally observed following the occurrence of a meteor. Both phenomena are thought to be produced by intrinsic emission mechanisms; PTs have been associated with chemiluminescent reactions between meteoric metals and atmospheric ozone whereas MRA emission arises due to radiation emitted by processes in the meteor's plasma trail. Previous research has identified an association between these phenomena, and proposed a mechanism by which the reactions responsible for PTs could also fuel MRAs. In this work, we investigate said connection using a substantially larger catalog containing hundreds of examples of each phenomenon. Using meteor data from the Global Meteor Network (GMN), we performed a directed search in all-sky radio images obtained by the Long Wavelength Array (LWA) radio telescope to identify meteors with MRAs. The resulting catalog spanned nearly 2 years and contained a total of 2,887 meteors, with 675 MRA events and 372 PTs. Statistical analyses suggest that the connection between the two phenomena is not as strong as previously supposed. Additionally, we show that the MRA occurrence rates do not have a strong seasonal dependence, meteoroid strength dependence, or preference between meteor showers and sporadics. Interestingly, we find that a meteor's entry angle appears to play a significant role in whether an MRA is observed.

1. Introduction

Though the initial luminous streak of a meteor typically lasts less than a couple seconds, meteors occasionally produce lingering trains which can exist for significant periods of time. These long-lasting trains are generated via self-emission mechanisms and can be broadly divided into two categories: those seen in visible and infrared wavelengths due to chemiluminescent reactions, known as persistent trains (PTs; Borovička, 2006), and those observed in radio frequencies potentially arising from resonant transition radiation or Langmuir waves, known as meteor radio afterglows (MRAs; Obenberger et al., 2020).

Because their train is visible to the naked eye, PTs have been observed and documented since nearly a millennium ago, though they did not begin to undergo rigorous scientific investigation until the early 1900s (Beech, 1987). Much of the current understanding about the formation and evolution of PTs was developed during the Leonid outbursts of 1999–2002; a variety of research endeavors were planned and carried out during this period (e.g., Higa et al., 2005; Jenniskens & Butow, 1999; Kelley et al., 2000). From these studies, it was found that meteor trains can experience up to three distinct stages in their evolution, namely the afterglow, recombination, and continuum phases (Borovička, 2006). The continuum phase, which typically begins after 30–40 s for Leonid meteors (Abe et al., 2004; Borovička & Koten, 2003), contributes most to the endurance of these trains and can last upwards of an hour (Beech, 1987). For clarity, the "PT" designation as we use it in this work applies specifically to those trains which endure long enough to exhibit continuum emission. Throughout their period of luminescence, trains can be observed to undergo complex morphological evolution in response to the neutral winds present in the mesosphere and lower thermosphere (MLT) region. In some instances, the train can appear as two distinct, parallel lanes of luminous material (known as "double trains"); these develop from counterrotating linear vortices in response to buoyancy effects (Zinn & Drummond, 2005) or convective instabilities (Kelley et al., 2013).

The PT spectrum observed during the continuum phase is generally absent of atomic spectral lines (excepting a potential minor contribution from the Na D-lines), and is instead dominated by band emission from molecules

Software: L. E. Cordonnier, K. S. Obenberger, J. Dowell, D. Vida
Supervision: K. S. Obenberger, G. B. Taylor, J. M. Holmes, J. Dowell
Validation: L. E. Cordonnier
Visualization: L. E. Cordonnier
Writing – original draft: L. E. Cordonnier
Writing – review & editing: L. E. Cordonnier, K. S. Obenberger, G. B. Taylor, J. M. Holmes, J. Dowell, D. Vida

(Borovička, 2006). Luminosity in the near-infrared (NIR) 700–900 nm range has been attributed to the $\left(b^1\Sigma_g^+\right) \rightarrow \left(X^3\Sigma_g^-\right)$ transition of $O_2(0,1)$ (Hapgood, 1980; Kruschwitz et al., 2001), though others suggest that OH transitions are instead responsible (Clemesha et al., 2001; Vasilyev et al., 2021). Additionally, heated atmospheric species such as CO, CO_2, CH_4, and H_2O have been identified in the mid-IR (MIR) 3–13 μm regime (Russell et al., 1998). For optical wavelengths, Jenniskens et al. (1998) asserts that the majority of emission arises from the "orange arc" band emission (West & Broida, 1975) of iron oxide (FeO) molecules in the 570–630 nm window. This FeO can be produced by reacting ablated meteoric Fe with atmospheric ozone according to:

$$Fe_nX + O_3 \rightarrow FeO^* + O_2 + Fe_{n-1}X \tag{1a}$$

$$FeO + O \rightarrow Fe + O_2 \tag{1b}$$

where Fe_nX is an Fe-containing cluster with X representing other meteoric metals/metal oxides. This reaction could also proceed with atomized Fe instead, in which case Fe_nX is replaced with Fe and the $Fe_{n-1}X$ term vanishes; under these conditions reaction 1a is exothermic by approximately 26,000 cm^{-1} and the excited FeO^* can easily populate the $D^5\Delta$ and $D'^5\Delta$ states (Lei & Dagdigian, 2000). These states have previously been identified in the PT continuum emission (Jenniskens et al., 1998; Popov et al., 2020). It has been proposed that other meteoric metals (e.g., Ca and Mg) are also capable of participating in similar oxidation reactions as shown in reaction 1 (Baggaley, 1976). In concluding this discussion of PT chemistry, it is important to emphasize that much work still needs to be done to verify that this outlined mechanism applies to the entire population of PTs and not just to those associated with the Leonid meteors.

Cordonnier et al. (2024) recently compiled a catalog containing 636 meteors with trains over a period spanning nearly 2 years which, unlike previous catalogs, was shower-agnostic and was observed and reduced with the same equipment/pipelines. This catalog revealed that many of the previously held assumptions about PTs were not broadly applicable, including restrictions on the parent meteor's velocity and brightness. Instead, a meteor's altitude (specifically its ending altitude) was found to be the most significant indicator for whether a PT could exist. This is not entirely unexpected, as it has been well-documented that PTs exist in a very narrow altitude range —roughly between 85 and 95 km (Cordonnier et al., 2024; Trowbridge, 1907; Yamamoto et al., 2004). This range neatly coincides with the secondary ozone maximum (Smith et al., 2013); ozone, as suggested by reaction 1, is a necessary reactant for chemiluminescence. The natural semiannual variation in the concentration of ozone within this region of the atmosphere was found to significantly affect the monthly occurrence rate of PTs, indicating that PTs are closely tied to this ozone and could potentially be used as a means to estimate it (Cordonnier et al., 2025a). Results from the PT catalog also indicate other factors which appear to play a role in PT formation, including: dynamic origin (material from Jupiter family comets is most fruitful), K_B parameter of meteoroid strength (weaker material produces more PTs), and material recency (meteoroids corresponding to "recent" parent body fragmentation events have higher PT occurrence rates). In this present work, we utilize the meteor data from this catalog (Cordonnier et al., 2023) as the basis for our MRA search.

Unlike PTs, the MRA phenomena was only recently discovered by Obenberger et al. (2014) using the first station of the Long Wavelength Array (LWA1; Ellingson et al., 2013) which is co-located with the core of the Karl G. Jansky Very Large Array (VLA) in New Mexico. These early MRA detections were associated with meteors brighter than visual magnitude −3.3 (i.e., the realm of fireballs); these MRAs exhibited light curves characterized by a fast rise and exponential decay lasting tens of seconds up to a few minutes (Obenberger et al., 2014). From an observational standpoint however, meteors fainter than this do not always clearly demonstrate this pattern as their emission can occur on timescales comparable to or less than the integration time of the radio telescope (e.g., those seen in Dijkema et al. (2021) and this work). The archetypal MRA produces emission which is broadband (detected between 20 and 60 MHz so far), largely unpolarized, and has a smooth spectrum (Obenberger et al., 2015). When the spectra are fit to a power law, the spectral indices have ranged from flat to steep—a sample of 86 MRAs had a spectral index distribution which peaked at −1.73, though many spectra were better modeled by a log-normal function with a turnover between 30 and 40 MHz (Varghese et al., 2021). Spectral indices have also been observed to undergo temporal evolution, gradually steepening with time likely due to the diffusion of the train (Obenberger, Dowell, et al., 2016). The radiation pattern of MRAs has been shown to be isotropic (Varghese et al., 2019) with no small-scale regions of coherent emission down to sizes of at least ∼1 km (Varghese et al., 2024). Lastly, the altitudinal distribution of MRAs exhibits a sharp cutoff below about 90 km

(Dijkema et al., 2021; Obenberger, Holmes, et al., 2016); this is likely related to atmospheric conditions which hinder electron motion, such as high collision frequencies and/or short mean free paths arising from the increase in atmospheric density.

After the initial detection of MRAs by LWA1, other radio telescope observatories were used to search for and detect this phenomena. This includes, in order of published detection, the Sevilleta station of the LWA (LWA-SV; Cranmer et al., 2017) located at the Sevilleta National Wildlife Refuge in New Mexico which has previously observed approximately 100 MRAs (Obenberger et al., 2020; Varghese et al., 2019, 2021) in addition to the 675 presented in this work. The LOw Frequency ARray, or LOFAR (van Haarlem, M. P. et al., 2013), is a European telescope with its core in the Netherlands; a campaign carried out during the 2020 Perseids meteor shower resulted in the detection of over 200 radio trails (Dijkema et al., 2021). Most recently, the LWA station located at the Owens Valley Radio Observatory (OVRO-LWA; Anderson et al., 2019) in California was used to detect five MRAs with high angular resolutions better than 30 arcminutes, or equivalently, 1 km physical scales at an altitude of 100 km (Varghese et al., 2024). Notably, no MRAs were observed by the Murchison Widefield Array (MWA; Tingay et al., 2013), located in Western Australia, over its 322 hr survey (Zhang et al., 2018); this search was conducted at a higher frequency band (72.3–86.4 MHz) relative to the other campaigns, suggesting that MRA spectra may have a sharper cutoff outside the 20–60 MHz band than is suggested by a simple power-law (i.e., they may be better modeled by the log-normal function).

Though the emission mechanism behind MRAs has not been completely ascertained, several potential explanations have already been ruled out. This includes specular reflections from terrestrial sources (Obenberger et al., 2014; Varghese et al., 2019), whereby ground-based transmitters reflect off the meteor's plasma train and are detected by the radio telescope; these reflections would be narrowband and strongly polarized which does not match the broadband, unpolarized nature of MRAs. In a similar vein, non-specular echoes (i.e., those due to scattering rather than reflection) have also been discounted (Obenberger et al., 2014). Zhao et al. (2023) have suggested that the reflection of diffuse galactic emission may explain the MRA phenomena, however this framework can only account for spectral indices of -1.3 and flatter. While some amount of galactic reflection is to be expected, the large number of events which are much steeper than this value strongly suggest that this mechanism is not singly responsible. Indeed, MRAs appear to radiate from self-emission processes. These processes cannot be related to cyclotron emission, as the gyrofrequency of the geomagnetic field is much too low to account for the observed radio spectra (Obenberger et al., 2015). As it stands, there are currently two main theories which align with previous observations: the electromagnetic conversion of Langmuir waves and resonant transition radiation.

Langmuir waves, or electrostatic plasma oscillations, were first proposed as a potential emission mechanism by Obenberger et al. (2015), however the plasma waves themselves need to be generated before they can be converted into electromagnetic (EM) waves. To generate these Langmuir waves, an instability in the meteor's plasma trail is required. For instance, a bump-on-tail instability is created when the plasma is exposed to an electron beam; this mechanism is likely responsible for the 150 km radar echo phenomenon (Oppenheim & Dimant, 2016). Driving this instability necessitates a replenishing source of suprathermal electrons, which remains to be conclusively identified (though one potential avenue is discussed below). It has also been suggested that coherent or partially coherent Langmuir oscillations could be driven by the differential motion of fast-moving charges in Earth's magnetic field (Epstein et al., 2025). An alternative theory proposes that explosive meteoroid flares could engender Langmuir waves which then propagate along, and are constrained within, the waveguide formed by the meteor's plasma trail (Mathews & Djuth, 2017). Assuming that Langmuir waves develop, they can be converted into EM waves through a variety of processes (e.g., those in Cairns, 1988; Schleyer et al., 2014; Malaspina et al., 2012); this mode conversion can be aided by the meteor trail's steep density gradients. The resulting emission will generally be at the local plasma frequency, which is proportional to the square root of the electron density—owing to the inhomogeneous nature of the plasma trail, the electron density varies throughout the trail which effectively results a spectrum of frequencies (Obenberger et al., 2015). Langmuir wave conversion, however, is a coherent process (i.e., has intrinsic polarization) at spatial scales corresponding to individual coherent regions; regions of polarized emission have not been detected down to scales of about 1 km (Varghese et al., 2024) indicating that either the coherent regions are much smaller than this scale and add incoherently or that the emission loses its polarization as it passes through the surrounding media.

The other prominent explanation involves transition radiation, that is, radiation generated by the propagation of fast-moving, charged particles (e.g., electrons) in media with random inhomogeneities. Though this radiation is emitted over a range of frequencies, it exhibits a very strong peak in intensity near the plasma frequency—by several orders of magnitude compared to "background" frequencies (Platonov & Fleishman, 2002); this mode is known as resonant transition radiation (RTR). The total intensity of RTR is dependent on the spectrum of plasma density inhomogeneities (commonly taken to be a power-law), the velocity distribution of the ensemble of emitting electrons, and is inversely related to the strength of external magnetic fields (Platonov & Fleishman, 2002). Obenberger et al. (2020) first proposed that RTR may be responsible for MRA emission. This is an attractive explanation as the needed random inhomogeneities are produced naturally through plasma turbulence in the meteor trail (Chau et al., 2014). The amount of turbulence present in the trail depends on factors such as the atmospheric neutral wind velocities, the background ionosphere, and the meteor's mass, altitude, and velocity (Dyrud et al., 2011). For relatively large meteors, the presence of charged dust is also likely to have an effect on the turbulence scales (Chau et al., 2014). Similar to the Langmuir wave mechanism, RTR also requires a consistent source of suprathermal electrons over the lifetime of the MRA. Obenberger et al. (2020) has suggested one possible source of these hot electrons, whereby ablated particles from the meteor attach an electron and then undergo reactions with some variety of oxygen (O, O_2, or O_3) which eject the electron with energies of roughly a few eV:

$$AP_1^- + O_n \rightarrow e^- + AP_2 + X \tag{2}$$

where AP is an ablated particle (AP_1 and AP_2 may be different species, with X representing any byproducts) and O_n is either O, O_2, or O_3. It would only take a small fraction $\left(\sim 10^{-10}\right)$ of the estimated total available electron energy produced via reaction 2 to be converted into radio emission to match the observed MRA energies (Obenberger et al., 2020). While both RTR and Langmuir wave emission provide plausible explanations for the observed MRA phenomena, modeling and simulation work is needed in order to understand the extent of their respective contributions (if any) and to confirm whether their emission characteristics agree with observations.

The detection of four meteors which exhibited both MRAs and PTs led Obenberger et al. (2020) to suggest that there could be a link between the two phenomena. Indeed, this claim was strengthened by the spatial coincidence of MRAs and PTs with one another instead of with features of the parent meteor (such as flares). In one case, the MRA followed a relatively small (less than ∼400 m) bright region of the PT. They went on to suggest that the chemical reactions responsible for driving PT emission could, with anion reactants, also serve as a source of the suprathermal electrons needed by MRAs. It is likely that both phenomena, along with long duration nonspecular meteor echoes, are also influenced by charged dust within the trail which can slow diffusion and prolong the duration of the emission (Chau et al., 2014; Kelley, 2004; Varghese et al., 2021). This present work seeks to statistically investigate the relationship between PTs and MRAs using hundreds of examples of each phenomena. We utilize the catalog of PTs published in Cordonnier et al. (2024) along with data from the all-sky radio observations from LWA-SV over the same time period.

The remainder of the paper is structured as follows: Section 2 details the equipment and instruments used to collect our data, Section 3 describes the data processing pipeline and selection criteria, Section 4 discusses the results and implications of our observations, and Section 5 summarizes our findings and presents key takeaways. Two appendices provide additional details on the all-sky radio astrometric calibration (Appendix A) and the radio flux density calibration (Appendix B).

2. Equipment and Instruments

2.1. Widefield Persistent Train Camera (WiPT2)

The Widefield Persistent Train Camera 2nd Edition (WiPT2) was used to detect and obtain the PT data presented in Cordonnier et al. (2024); the complete description of the instrument and PT detection pipeline can be found therein, however we will summarize its key features and observational strategy here. The WiPT2 has been located at the Sevilleta National Wildlife Refuge in New Mexico since 5 October 2021, with the first data campaign lasting until 1 July 2023. During this span of 22 months, over 2810 hr of observations were collected. The WiPT2 employs a 61-megapixel IMX455 CMOS sensor with a Canon EF 15 mm f/2.8 fisheye lens resulting in a plate scale of ∼3.45 arcmin/pixel near zenith. The camera, sensor, and electronics are all contained inside a mini

refrigerator with a clear acrylic dome embedded in its top surface. The WiPT2 produced long exposure (5 s) images during moonless, nighttime conditions which were then binned into 4 × 4 superpixels before being processed through the meteor detection pipeline.

The meteor detection pipeline automatically identified transient, extended objects in the images. These identified objects were filtered based on whether they appeared in adjacent frames with similar properties (e.g., similar lengths, orientations, and closely separated) in an attempt to remove trails associated with airplanes and satellites. Additionally, any of the image sets which were dominated by clouds (per hour long increment) were removed from further consideration due to the large number of false positives they generated. The remaining events were manually reviewed to first verify that the object was indeed a meteor and second to determine whether any observable emission lingered after the initial meteor. This ultimately led to the detection of 849 meteors with trains, of which 636 were co-observed by the Global Meteor Network (see Section 2.3 below).

2.2. Long Wavelength Array—Sevilleta (LWA-SV)

As previously mentioned, the all-sky radio data for this work was obtained from the LWA-SV instrument (Cranmer et al., 2017), located at the Sevilleta National Wildlife Refuge (34.348358°N, −106.885783°E). LWA-SV is composed of an elliptical (100 × 110 m) pseudo-random distribution of 256 dual polarization dipole antennas, where each element is roughly 1.5 m tall and 3 m wide. An additional outrigger antenna is located ∼500 m west of the core for long-baseline calibration of the array. Underground cables carry signals from each antenna's front-end electronics into the electronics shelter, where the analog signals are digitized and processed. The array has a nominal frequency range of 3–88 MHz, and is capable of simultaneously operating in a beam-formed mode and the all-sky imaging mode, the latter of which is known as the Orville Wideband Imager, or simply "Orville" (Dowell et al., 2020). Orville is based on the Bifrost framework, which provides a high-throughput pipeline for correlating and imaging the all-sky data from LWA-SV (Cranmer et al., 2017; Varghese et al., 2021). The sky is imaged using a slant orthographic projection with an offset phase center (∼2° from zenith) to improve the speed of *w*-stacking (Varghese et al., 2021). This allows for 198 channels of 100 kHz each (19.8 MHz total bandwidth) to be imaged in 5 s integrations with full Stokes polarization products (Dowell et al., 2020); these are later averaged down to 6 channels of 3.3 MHz for archival purposes. The complete Orville data archive can be found at: https://lda10g.alliance.unm.edu/Orville/. Orville data is natively saved in a binary Orville Image Format (.oims) which encodes individual image frames and frame header information (Dowell et al., 2020); the .oims data products can be read and manipulated via Python scripts provided by the LWA collaboration (https://github.com/lwa-project/orville_wideband_imager).

All radio data analyzed in this work utilizes the archival 6 channel format. Between 5 October 2021 and 7 December 2022, Orville was primarily recording the sky between 21.7 and 41.5 MHz, however, after 7 December 2022 this range was changed to 29.8–49.6 MHz in order to avoid radio frequency interference (RFI) that was prevalent in the lower frequency channels. This 8.1 MHz shift in frequency is not an integer multiple of the channel bandwidth (3.3 MHz), meaning that the closest corresponding center frequencies in each observational period are offset by 1.5 MHz (e.g., the fifth channel in the first epoch, 34.9–41.5 MHz, is offset from the corresponding third channel in latter epoch, 36.4–43 MHz, by 1.5 MHz). Comparisons between derived radio parameters, such as spectral flux, between these two epochs are made using the nearest corresponding frequency channel.

2.3. Global Meteor Network (GMN)

The Global Meteor Network (GMN; Vida et al., 2019, 2021) represents the collaborative effort of a large number of amateur astronomers around the world, along with several professional institutions, to observe as many meteors as possible. The network consists of low-cost, high sensitivity CMOS video cameras which run open-source meteor detection software during nighttime conditions; as of mid-2025, there are over 1,300 cameras in 42 different countries. The computers attached to the cameras, typically Raspberry Pis, detect, calibrate, and record data for each meteor event. These data are currently being sent to a central server which performs event correlation between stations and calculates trajectory/orbital parameters, though plans to decentralize this process are underway. Central New Mexico is well-covered by GMN cameras: 20 are located within 100 km of the WiPT2 camera with a total of 51 stations contributing data to the PT catalog. The GMN database includes parameters relating to the atmospheric portion of the meteor flight (e.g., altitudes, duration, brightness, radiant, and entry

angle) as well as the pre-atmospheric, orbital information (e.g., Keplerian elements and derived parameters). These data comprise the foundation for the statistical analyses presented in Cordonnier et al. (2024) and we similarly rely on them heavily in this present work. It should be noted that GMN peak meteor magnitude values are not corrected for saturation effects. Reported peak magnitudes brighter than about −1 mag should be thought of as a hard lower limit rather than an accurate value (Vida et al., 2021); an individual meteor's apparent angular velocity will modify the actual saturation limit, but the −1 mag cutoff is a handy rule of thumb. Owing to this limit, the photometric mass (which is calculated using the meteor's magnitude) will also be underestimated when the GMN cameras become saturated. In such cases, the reported mass is also representative of a hard lower limit on the true mass.

3. Orville Data Processing

The catalog of meteors observed by the WiPT2 camera (Cordonnier et al., 2023) was used to direct the search for MRAs; this database contains a total of 4,726 meteors (of which 636 had optical trains). This strategy was preferred to a blind search because it greatly increased the probability that any detected radio transients were actually caused by meteors (as opposed to airplanes and scintillation). It also ensured that the resultant meteors had corresponding GMN data, which is important for the statistical analyses that follow. We retrieved the Orville data files, typically saved in hour-long blocks, corresponding to the time of each meteor (if the file existed). This resulted in a collection of 1,487 files (∼1.5 TB) which were subjected to the pipeline described in this section. Simply put, the MRA detection pipeline involved examining the all-sky radio data at locations/times of known meteors to determine whether any self-generated emission was produced.

The first step in this process was to use the sky coordinates of each meteor to calculate the corresponding pixel locations in the radio images. GMN data includes the beginning and ending location of the optical meteor in geodetic coordinates (i.e., latitude, longitude, and altitude above the WGS84 ellipsoid), which can easily be converted into a horizontal (altitude/azimuth) coordinate system based at the LWA-SV site by using the Python package pymap3d. It is possible to do the conversion from these sky coordinates into pixel locations using the astrometric parameters which are contained in the Orville file's header information. In practice, however, the mapping generated using these values led to offsets which were deemed too great for the accuracy desired in this work (e.g., 10% of tested points were discrepant by more than 1°, and 65% by more than 0.5°). Instead, an empirical astrometric model was created which minimized the discrepancy between a source's observed and calculated positions—this process is detailed in Appendix A. The improved mapping typically has offsets of less than 0.5° (93% of tested points), with 98% of tested points being discrepant by less than 1°. This level of accuracy was deemed sufficient for our purposes.

In order to detect transient phenomena such as MRAs, the Orville images need to be background subtracted. This process is simplified since this is a directed search rather than a blind search—we know the time at which the meteor occurs. Due to the potential for RFI and the inherent instrumental low sensitivity near the horizon, we only considered MRA emission which occurred above elevation angles of 30°. The pixel-by-pixel median of the four frames (20 s) directly preceding the meteor was computed to produce the background image. This process (and all that follow) was performed independently on all six frequency channels. We opted to use the median rather than mean as this reduces the impact of spurious frames, such as those affected by strong scintillation or RFI; we took four frames as this struck a good balance between removing short term fluctuations while not introducing much smearing. The background image is subtracted from the frame of the meteor and the subsequent 12 frames (covering 60 s post-meteor). For each of the background subtracted frames, the median absolute deviation (MAD) of the frame was calculated via $median(|X - median(X)|)$ where X is the flattened array of image values. The MAD was used as the metric for determining significance levels. We opted to use MAD rather than standard deviation because MAD is more robust against outliers, which abound near the bright radio sources (primarily due to the magnitude of scintillation they undergo); these outliers would greatly skew the standard deviation but have negligible effect on the MAD. In general, values greater than 5 ×MAD were considered "significant" for the purposes of MRA classification (see bullet point 2 below). On average, approximately 2.5% of pixels per non-MRA image will satisfy this significance condition, though many of these are associated with the bright radio sources, that is, Cygnus A (Cyg A), Cassiopeia A (Cas A), Taurus A (Tau A), Virgo A (Vir A). By excluding the pixels in the neighborhood of these sources, this number is reduced to about 1.5%. We expect that many of the remaining significant pixels are caused by a combination of ionospheric scintillation of the multitude of dimmer radio sources and radio emission (or reflection) by terrestrial sources such as airplanes.

To verify that any potential MRAs were indeed of meteoric origin rather than scintillating background sources serendipitously aligned with the path of the meteor, the Very Large Array Low-Frequency Sky Survey Redux (VLSSr) catalog was employed (Lane et al., 2012, 2014). The VLSSr catalog of sources was produced at a frequency of 73.8 MHz, which is above the maximum frequency covered in this study (49.6 MHz); despite this, we make the assumption that the VLSSr flux data is broadly mappable to our frequency band (within a factor of a few or so). A similar generalization was used by Varghese et al. (2021) in their examination of MRAs at our frequency range. In order to compare the magnitude of flux between potential MRAs and nearby VLSSr sources, the Orville images needed to be flux calibrated. This process is detailed in Appendix B which, after calibration, enables pixel values to be converted into spectral flux values. In the absence of scintillation, steady radio sources will be entirely removed during the background subtraction process meaning that any remnants left behind are the result of scintillation. The amount of scintillation depends on the state of the ionosphere, which is affected, for example, by the time of day and the solar cycle (n.b. all radio data analyzed in this work occurred at night). Based on the data displayed in Figure B1 in Appendix B, it is not unusual for Cyg A to be appear twice as bright as its nominal value (98% of observations are less than twice the modeled value); assuming that similar levels of enhancement are possible for other sources, they would (at most) appear to be their respective nominal fluxes in the subtracted images. For each potential MRA, the position of maximum flux was noted. If any VLSSr sources were located within 3° of this position which had fluxes comparable to the observed flux, then the object was flagged as indeterminate and was removed from further analyses. In many cases the path of the meteor coincided, either partially or totally, with the bright radio sources (e.g., Cyg A and Cas A); these events were also excluded from consideration due to the variability of these sources.

Once the external influences have been removed, the remaining task is to determine whether the emission, now solidly associated with the meteor, arose intrinsically or from the reflection of terrestrial transmitters. Transmitter echoes are generally narrow band (∼kHz scale) and have strong polarization; this makes them relatively easy to flag in observations which have high frequency resolution, such as the 198 channel Orville data. A handful of these 198 channels contain known RFI sources which have been identified previously; these bad channels are flagged and removed prior to the data being averaged down into the six channel archival format. This flagging is not dynamic however, meaning that any strong transmitter echoes in one or more of the remaining channels will be propagated through into the final archival data. This makes it slightly more challenging to say definitively whether a particular archival channel is dominated solely by meteor emission or if the intensity/polarization has been modified by the presence of reflection echoes. For this reason, we implemented the following criteria for determining whether the emission in each frequency channel should be attributed to MRAs or specular reflections (or neither):

1. If the total polarization fraction during peak emission exceeds 0.5, the channel was disregarded since it likely had moderate to severe contamination by reflection(s). While most previous MRAs have shown little polarization, we allowed for the relatively high 50% cutoff as some quantity of reflection is inevitable under this data archiving strategy.
2. After discounting the high polarization channels, the remaining channels' MAD values at the time of peak emission were collected and their median was computed. If this value was less than 5, the emission was deemed to have insufficient significance. We opted to do this wholistic approach rather than examining the MAD of individual channels as this provided a single decision metric and did not prioritize the significance of any single channel over the rest.
3. If the region of emission was not located within the path of the meteor (or very near to it, less than $\sim 1°$), then the event was discarded. Similarly, the emission had to be localized with respect to the meteor path in order to be considered an MRA.
4. The qualitative profile of the light curve was also taken into consideration. MRA light curves conventionally exhibit a fast rise and exponential decay (e.g., Obenberger et al., 2014), though this behavior can be harder to distinguish in dimmer events. If our light curves did not exhibit an obvious peak which was consistent with a general rise and decay profile, then the event was excluded.
5. We required that at least three of the six frequency channels were consistent with emission from MRAs. This does not necessarily imply that the remaining channels were dominated by reflection echoes or irregular light curves; it was not unusual for a couple of the channels to be “dead” and as such contain no data.
6. Ultimately, borderline events which came down to subjective judgment were removed, erring on the side of caution.

Of the 4,726 meteors in the original optical catalog, 3,340 were congruous with the elevation-masked radio data—that is to say, these meteors occurred at a time and sky location where (a) Orville data existed, and (b) any emission, if present, occurred above the 30° elevation angle cutoff. Furthermore, we were able to confidently classify 2,887 of these meteors with regard to the presence MRA emission; the remaining 453 events were indeterminate due either to nearby source confusion or the presence of emission which was not consistent with MRAs but was too significant to warrant a null classification. These 2,887 meteors, with 675 MRAs and 372 PTs, form the basis for all ensuing analyses.

4. Results

In this section, we will investigate a multitude of MRA properties, both in relation to previous literature and to PTs.

4.1. Altitude

The altitude corresponding to the brightest region of the MRA at 38 MHz was computed following the technique of Cordonnier et al. (2024). If the channel containing 38 MHz was deemed unusable (due to RFI, meteor reflections, or no data), then the nearest usable channel was chosen instead. The geodetic coordinates corresponding to the start and end of the optical meteor, as determined by the GMN, were first converted into Earth-centered, Earth-fixed (ECEF) coordinates. These coordinates were connected by a line segment which was discretized into 5,000 points. Each of these points was then converted into an altitude/azimuth coordinate; the pixel location corresponding to the maximum of the MRA was also converted into an altitude/azimuth coordinate following the astrometric conversion detailed in Appendix A. The angular separations between the sky positions of the MRA and the 5,000 points were then computed. Whichever point had the smallest angular separation was taken to represent the peak location of the MRA, which was then converted from an ECEF coordinate back to a geodetic coordinate thereby providing the height above the WGS84 ellipsoid. There are two main sources of error to consider for this altitude calculation: the astrometric error of the MRA arising from the imperfect mapping from pixel to sky position and the ambiguous location of the maximum within the pixel. The latter consideration stems from the assumption that the true maximum occurs at the center of the pixel; the average size of a pixel in the all-sky images is $\sim 1.2°$ for elevation angles greater than 30°, resulting in an intrinsic uncertainty of approximately 0.6°. We opted for this approach primarily due to its simplicity—higher accuracy, if desired, could be obtained by using techniques such as 2D interpolation instead. Based on the improved astrometric data shown in Appendix A, we assumed a conservative error of 0.5° originating from imperfect astrometry. These two errors are generally expected to be independent, so they were added in quadrature for an overall error of 0.78°. Accordingly, we found the two points along the discretized line segment which were separated from the fiducial MRA point by 0.78° and then converted them into altitudes in the same manner. These set the upper and lower altitudinal bounds. The larger of these two values was combined in quadrature with the 3σ error in GMN meteor height; this value was taken to be the representative altitudinal uncertainty. Nearly 95% of these uncertainties were 2 km or less, with an average uncertainty of 1.2 km.

The MRA peak heights calculated here are consistent with the distribution seen in Obenberger, Holmes, et al. (2016). There is a sharp decline in the number of events which peak below altitudes of ~90 km; of the 675 MRAs, 15% had peak intensities occurring below 90 km and only 2% peaked below 87 km. The lowest recorded event had a peak height of 81.7 ± 1.4 km. The distribution of the peak MRA altitudes is shown in Figure 1. In contrast, the overall optical meteor population considered in this work routinely peaked below these altitudes, with 47% having their greatest brightness below 90 km and 11% having it below 80 km. All MRA parent meteors in our study began above an altitude of 86 km; this provides a convenient cutoff which can be used to normalize on the basis of altitude. The mean peak height for our MRAs was 95.5 km with a standard deviation (σ) of 5.2 km. This altitudinal range aligns fairly well with that of PTs—the altitude where PTs typically begin (93.2 km, $\sigma = 3.8$ km) occurs just below the typical peak height of MRAs (Cordonnier et al., 2024). Owing to this, the 131 meteor events which exhibited both an MRA and PT had an average peak MRA altitude of 91.5 km ($\sigma = 3.4$ km), which is 4 km lower relative to the overall population. This is not entirely surprising, as each phenomenon's formation is known to be strongly dependent on altitude; while MRAs appear to have only a lower altitude cutoff (Obenberger, Holmes, et al., 2016), PTs are altitudinally constrained both above and below due to the availability of atmospheric ozone (Cordonnier et al., 2024).

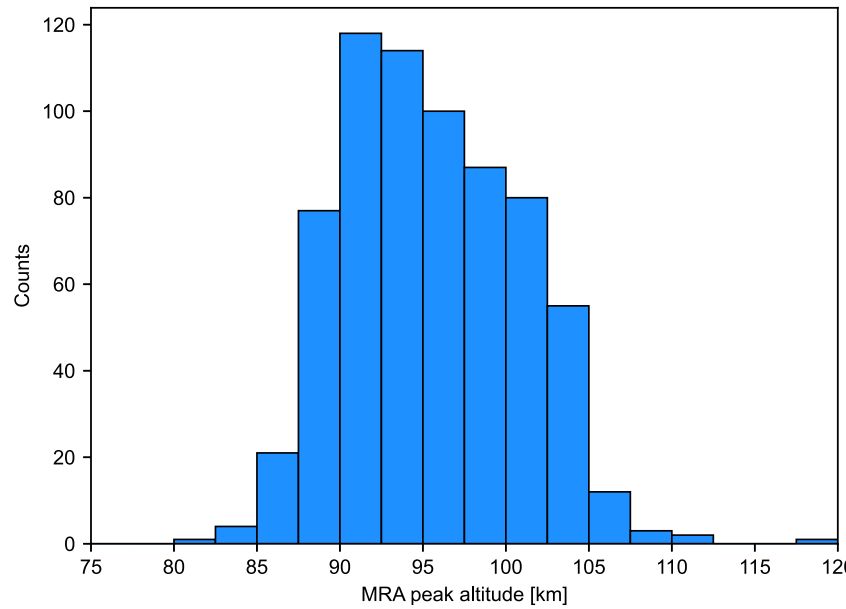

Figure 1. Histogram of MRA peak altitudes. There is a noticeable decrease in the number of MRAs which peak below ~90 km, in agreement with Obenberger, Holmes, et al. (2016).

4.2. Spectral Index

From the outset, the spectra of MRAs have been described by a power law of the form $S_\nu \propto \nu^\alpha$, where S_ν is the flux density at a given frequency ν and α is the spectral index. The spectral index has been found to vary with time, getting steeper (more negative) as time goes on due to the diffusion of the trail (Obenberger, Dowell, et al., 2016). Accordingly, we opted to compute α using the time and pixel corresponding to the MRA's maximum intensity at or around 38 MHz. During the first frequency epoch, this corresponded to the $34.9-38.2$ MHz channel, and during the second, the $36.4-39.7$ MHz channel. In cases where these channels were dominated by meteor reflection rather than emission, the nearest clean channel was used instead. We determined the flux densities and uncertainties as per Appendix B; these were then fit to the above power law, weighting the fit based on the individual uncertainties. Unlike previous studies which calculated α using the high spectral resolution data (i.e., 198 channels), our data relies on 6 channels at best, and at worst, only 3. Though efforts were undertaken to flag/remove the channels which were clearly dominated by meteor reflection, it is all but certain that instances remain where the MRA intensity has been at least partially modified by terrestrial reflection and/or RFI. Therefore, due to this consideration and the small number of data points, the reported spectral indices that follow are not as tightly constrained as those described in previous research.

Figure 2 shows the spectral index distribution using 649 MRAs; the remaining 26 events were not able to be flux calibrated due to insufficient calibrator data. This distribution peaks at $\alpha = -2.92$, which is steeper than the peak value that Varghese et al. (2021) obtained ($\alpha = -1.73$) for their sample of 86 events. It is, however, less steep than the spectral indices obtained in previous studies for bright meteors, which are typically steeper than -4 (Obenberger, Dowell, et al., 2016; Obenberger et al., 2015; Varghese et al., 2024). Nine of our MRAs had spectral indices which were positive—inverted spectra have not been previously observed for MRAs, though care must be exercised here as the small number of fitted points and susceptibility to inextricable RFI/terrestrial reflection could ultimately be responsible for this odd population. Higher frequency resolution would be necessary to confirm the existence of an inverted spectrum MRA. Varghese et al. (2021) broadly found that spectral index values were not strongly correlated with any of the physical meteor/MRA parameters they tested (e.g., altitude, entry angle, and energy). In the same vein, we performed a two-sample Kolmogorov–Smirnov (KS) test to determine whether the spectral index distribution for events having only MRAs differed significantly from those which had both MRAs and PTs. Based on this test, there is an apparent distinction between these two samples (p-value: 0.001), with events having both phenomena tending towards slightly flatter spectral indices. However, this result is misleading—there exists a weak correlation between the altitude of an MRA and its spectral index, with

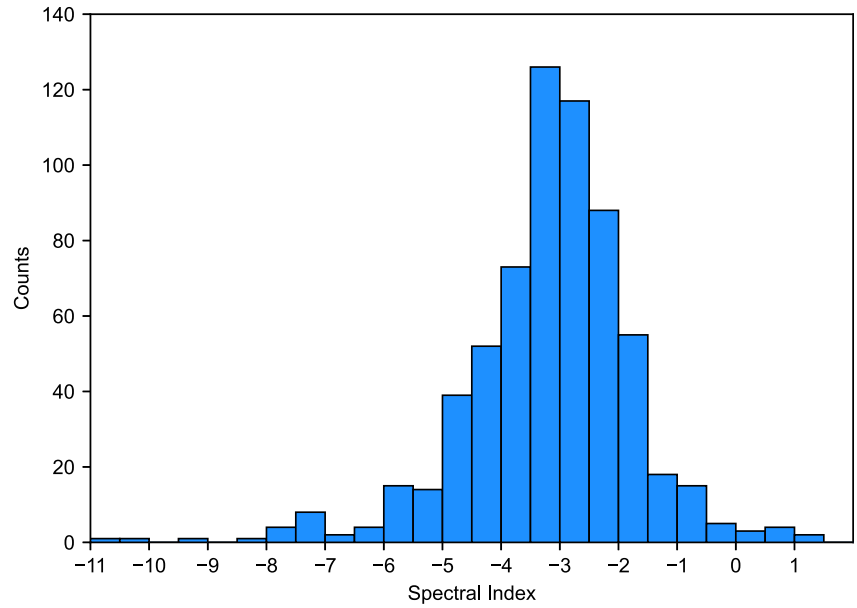

Figure 2. Histogram of MRA spectral indices. The distribution has a peak spectral index of −2.92.

low-altitude MRAs having flatter spectral indices. At high altitudes, a meteor's plasma trail diffuses more rapidly which means that there will be less plasma emitting at the higher plasma frequencies; this leads to a steeper spectral index. Varghese et al. (2021) detected this trend as a weak, tenuous correlation with a Pearson correlation coefficient of −0.07 (p-value: 0.72), which our sample strengthens to −0.13 (p-value: 0.001). Since PTs preferentially occur at low altitudes in the MRA zone, they are biased towards flatter spectral indices; repetition of the KS test accounting for this altitude dependence entirely removes this spectral index distinction (p-value: 0.79). This test was done using only meteors which had MRA altitudes below 93.2 km, that is, the average upper altitude at which PTs form (Cordonnier et al., 2024). Therefore, despite the statistically significant difference from an observational standpoint, there does not appear to be a significant physical relationship between spectral index and PT formation.

4.3. Turnover Frequency

Varghese et al. (2021) found that the spectra of MRAs, in many instances, can be better modeled by a log-normal distribution of the form:

$$S_\nu = Ae^{-\frac{(\log\ \nu - \log\nu_0)^2}{2\sigma^2}} \tag{3}$$

where ν_0 is the turnover frequency, A is a scale factor, σ is the standard deviation, and S_ν is the flux density at a given frequency ν. There are two main observation-oriented benefits arising from a log-normal model. First, it ensures that flux density does not grow arbitrarily large at low frequencies, and second, it aligns with the null detection of MRAs by the MWA at higher frequencies. If MRA emission truly followed a power law, their spectral indices would need to be steeper than −3.7 in order to be consistent with a null detection by the MWA at a 95% confidence limit (Zhang et al., 2018). Between this work and Varghese et al. (2021), there are hundreds of events flatter than −3.7, indicating that the power law formulation must not hold at higher frequencies. A log-normal distribution, on the other hand, could resolve this issue as it can decay much quicker than an equivalent power law.

We show the distribution of turnover frequencies for each frequency epoch in Figure 3. The LWA's frequency bandpass is indicated by the shaded regions; MRA events occurring within these shaded regions therefore had observed log-normal turnovers. Turnovers occurring far outside the shaded regions required extrapolation and are therefore less reliable, that is, their associated MRA spectra may not be best described by a log-normal model. Out of the 407 MRAs which could be fit to a log-normal distribution, 175 (43%) showed turnovers within the

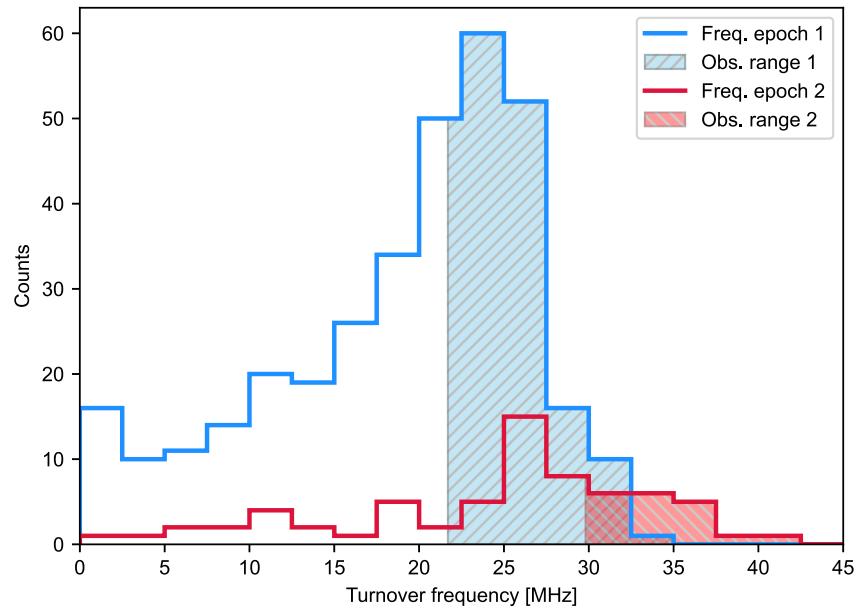

Figure 3. Histogram of MRA turnover frequencies derived from a log-normal fit for the two frequency epochs. The shaded regions indicate the frequency range over which the LWA was observing during each respective epoch: 21.7–41.5 MHz in epoch 1 and 29.8–49.6 MHz in epoch 2. A combined 43% of MRAs show log-normal turnovers within the observational frequency range.

bandpass. Varghese et al. (2021) found a weak positive correlation between the turnover frequency and the height of the MRA, with a Pearson correlation coefficient and two-tailed p-value of 0.31 and 0.14, respectively. This behavior is the opposite of what is expected, as low frequencies are less readily absorbed at higher altitudes, which ought to result in lower turnover frequencies. They note, however, that the unexpected correlation may be spurious, owing to the large p-value and small sample size. We repeat their analysis using our calculated log-normal turnovers and MRA peak altitudes—including all data (407 events) results in a Pearson correlation coefficient of -0.075 (p-value: 0.13). If we include only those events which have relatively well-constrained turnovers, that is, those with standard deviation errors less than 10 MHz (351 events), then the Pearson correlation coefficient becomes -0.11 (p-value: 0.04). A scatter plot of the latter sample is shown in Figure 4. The correlation coefficient remains negative regardless of whichever arbitrary standard deviation cutoff is used. This analysis suggests that these two quantities do indeed have a weak negative correlation, in accordance with expectations. That is to say, higher altitudes should have lower plasma frequencies due to the diffusion of the trail; we expect MRA emission to be reflective of said plasma frequencies in both the Langmuir and RTR hypotheses. The decrease in turnover frequency with altitude is therefore consistent with this notion.

4.4. Time of Year

Previous work by Cordonnier et al. (2025a) has demonstrated that the PT occurrence rate among sporadic meteors has a clear semiannual trend which aligns well with the trend exhibited by mesopause ozone. The relationship between these quantities stems from the chemiluminescent mechanism responsible for PTs (viz. reaction 1), whereby the chemical composition of the atmosphere appears to play a significant role in the formation of this phenomenon. Naturally, the question arises as to whether MRAs also exhibit variability in their occurrence rates. This variability, if present, would not be expected to directly depend on the atmosphere's chemical composition, but rather on factors such as electron density, collisional frequency, atmospheric turbulence, and the like. In examining the temporal variability, we consider only non-shower (sporadic) meteors as they are expected to be more representative of a diverse, unbiased sample than shower meteors. Meteors within each shower will broadly have the same physical and orbital parameters; if a given shower has characteristics which are particularly favorable/unfavorable for MRA formation, then any occurrence rate derived using these data would be skewed. Similarly, we compute the occurrence rates including only meteors which began above 81.7 km, as this is the lowest height at which an MRA's peak was observed. Meteors which began below this altitude are likely to be

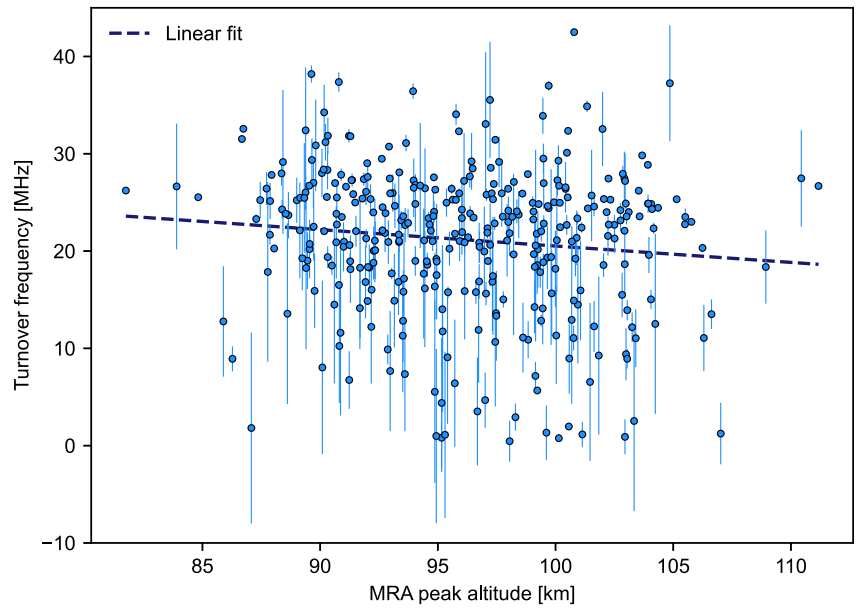

Figure 4. Scatter plot showing the relationship between the log-normal turnover frequency and the altitude at which the MRA exhibited peak intensity. Only turnover frequencies with standard deviation errors less than 10 MHz are included (the one sigma errors are depicted by the error bars). The typical altitudinal error is less than ∼2 km. These points have a Pearson correlation coefficient of −0.11 with a two-tailed p-value of 0.04. The dashed line indicates the best linear fit to these data, given by $y = -0.17x + 37.35$.

outside the "MRA zone" and as such are excluded in order to normalize the data to only consider meteors which could have formed MRAs.

Figure 5 shows the temporal variation in MRA occurrence rates among sporadic meteors for two different time-binning regimes: monthly and quarterly. The red shaded region denotes the 95% confidence interval for the calculated MRA occurrence rate; this was range was computed as per Cordonnier et al. (2025a) by assuming that the observed number of MRAs per time period is drawn from a Poisson process. As such, the confidence interval for the number of MRAs per time period is given by $[\Pr(\alpha/2, 2x)/2, \Pr(1-\alpha/2, 2(x+1))/2]$ where Pr is the percent point function of the χ^2 distribution, x is the number of observed MRAs, and α is the chosen significance level ($\alpha = 0.05$) for the confidence interval (Ulm, 1990; Vida et al., 2023). These bounds were then divided by the fiducial number of sporadic meteors observed during the same period in order to arrive at the MRA occurrence rate confidence interval. The large interval associated with the July 2022 point is a direct consequence of the small number of observed events for the month, with only 2 MRAs in 10 meteor events. The monthly binned panel of Figure 5 does not suggest the presence of any strong annual or semiannual trends. The apparent oscillations with a ∼2 month period are interesting, however it is unclear at this resolution whether they represent a physical process or are simply an artifact of small number statistics; the associated confidence intervals overlap to a degree such that this distinction is untenable. Presently, our temporal resolution is limited by small number statistics within each interval. Increasing the number of meteors and MRAs observed per interval would enable the occurrence rates to be determined more accurately and/or with higher temporal resolution, which would shed more light on the physicality of this trend. This could easily be accomplished, for instance, by incorporating data from the other existing (and planned) LWA stations.

The coarse, quarterly binned data in Figure 5 hints at an overall decrease in the occurrence rate of MRAs over our nearly 2 year long campaign; while this trend is more convincing than the bimonthly oscillations, its physical interpretation is no clearer. This is due, in part, to Orville's changing sensitivity over the duration of the campaign (as detailed in Appendix B) which could potentially influence the MRA detection sensitivity—in which case, the decreased occurrence rate could simply be attributed to instrumental bias. Long-period modulations of the MLT/ionosphere, such as those driven by the 11-year solar cycle, could also contribute, however we reserve such speculation until we are certain that instrumental contributions are not responsible. Therefore, unlike PTs, MRA occurrence rates appear to have no conclusive temporal dependence on timescales exceeding ∼months, though

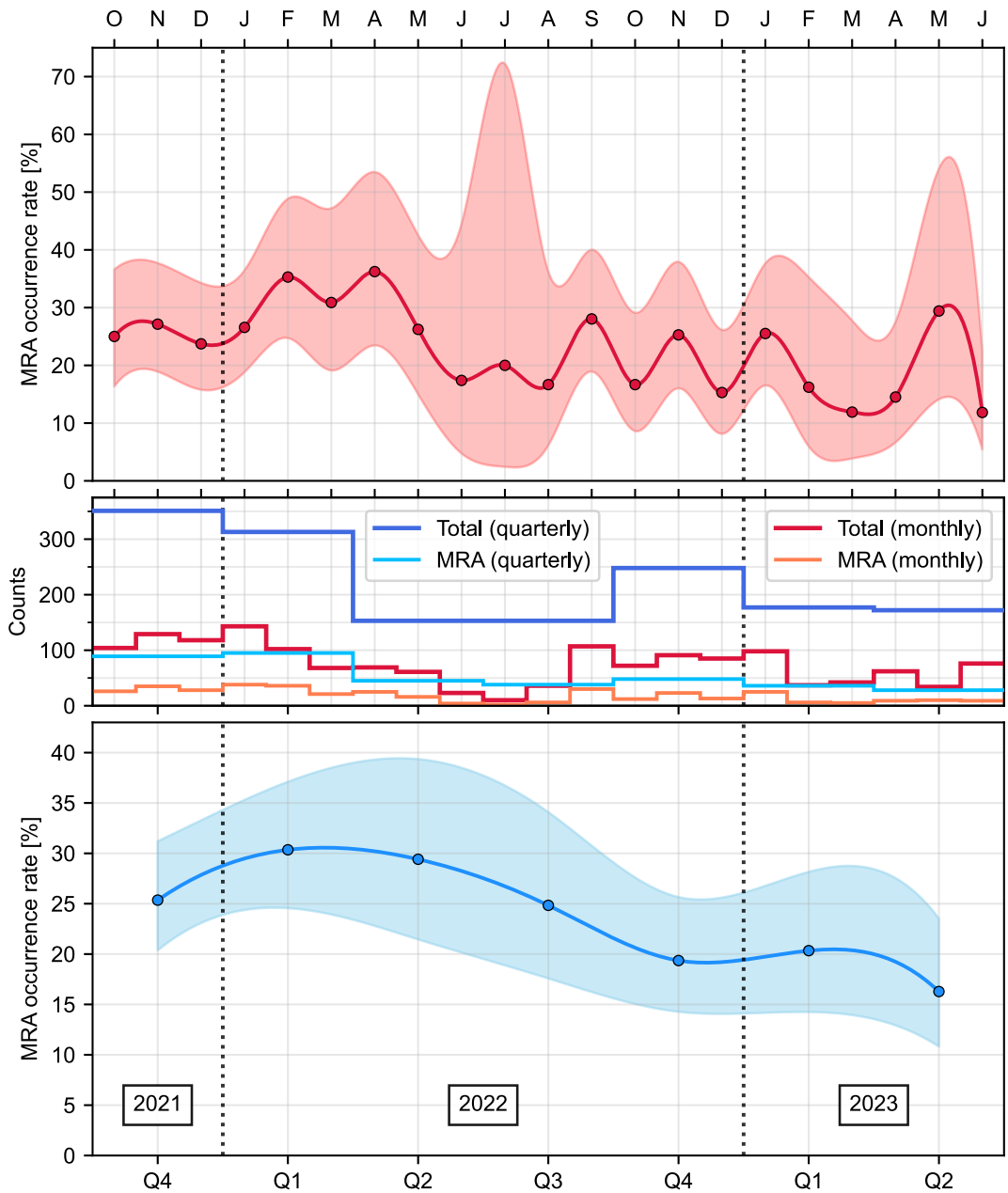

Figure 5. MRA occurrence rates among sporadic meteors binned monthly (top) and quarterly (bottom). The shaded region indicates the associated 95% confidence interval. Data points and the confidence interval have both been connected using cubic interpolation. No definitive trends are seen on short timescales (e.g., no semiannual oscillations), though the coarse quarterly binning suggests a potential overall decrease in MRA rates. (middle) Histograms showing the total count of sporadic meteors beginning above 81.7 km and their associated MRAs for both the monthly and quarterly binning.

additional data and comparisons between LWA stations would aid in validating this assertion. The detection methodology employed herein necessarily precludes MRAs which occurred during daytime hours, meaning that investigations into short, diurnal variability are not presently possible. MRAs can and have been readily detected during the day; data presented in Varghese et al. (2021) suggest the presence of a diurnal response, however further work is needed to confirm and characterize this trend.

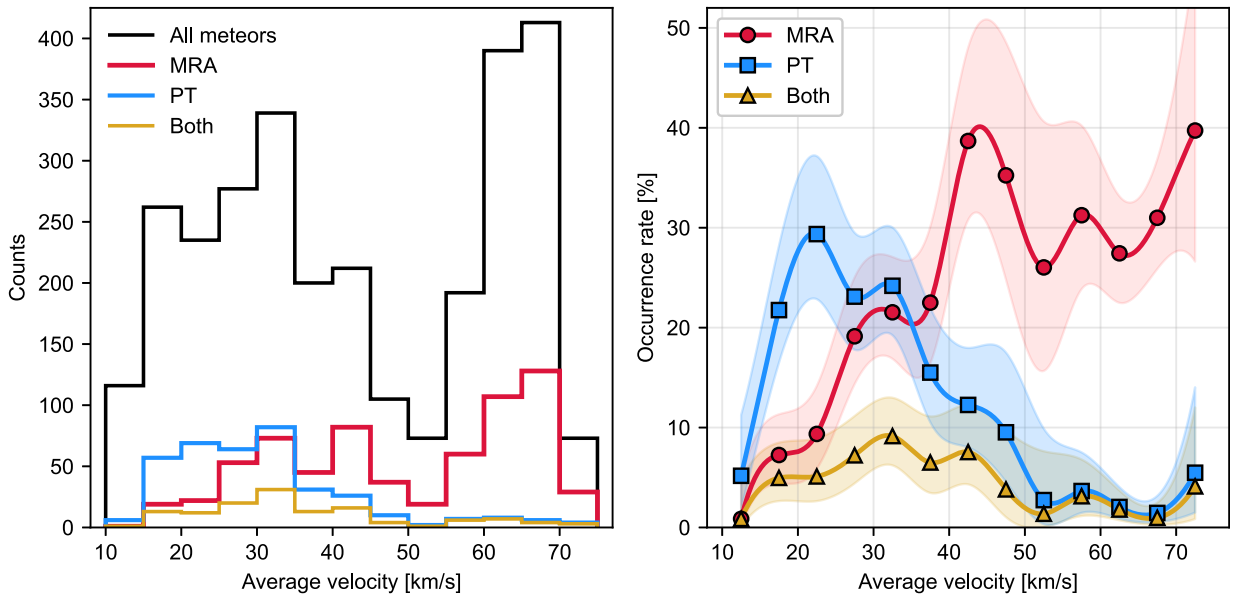

Figure 6. (left) Histogram of events using a bin size of 5 km/s. "All meteors" includes all meteor events observed in this campaign. The "MRA" and "PT" distributions indicate the number of events with each respective phenomenon; since these phenomena are non-mutually exclusive, events exhibiting both MRAs and PTs are also included in each histogram. The "Both" distribution explicitly plots those events which had both MRAs and PTs. (right) The percentage of events within each velocity bin exhibiting the indicated phenomenon. The shaded regions show the 95% confidence interval for each point (described in text); data points and confidence intervals have been smoothly connected via cubic interpolation.

4.5. Velocity

Meteors which have lower average velocities form PTs more readily than their faster counterparts, though this dependence likely has less to do with the intrinsic velocity per se and more with parameters which affect and are affected by velocity (Cordonnier et al., 2024). For instance, meteor velocity influences the range of altitudes where ablation occurs, with altitude being of paramount importance for PTs; similarly, the meteoroid's dynamic origin (and orbital properties) dictate which velocities are accessible, for example, meteoroids originating from the asteroid belt tend to have slower entry velocities compared to those originating from the Oort cloud. Since chemiluminescence drives PT emission, these factors which govern the chemistry and conditions of the reactions (altitude range and meteoroid composition, e.g.) will dominate—meteor velocity, in this case, serves primarily as a proxy. The emission from MRAs, on the other hand, is thought to arise from processes occurring in the plasma trail produced during a meteor's entry. Meteor velocity, for instance, affects the amount of turbulence generated (Dyrud et al., 2011) and the ionization efficiency, which goes as $\sim v^5$ per gram for a given entry velocity, v (Whipple, 1955).

Figure 6 shows the relationship between meteors' average velocity and the production of MRAs/PTs. The average velocity values are obtained from the GMN and represent the meteors' apparent ground-fixed average velocity over the luminous portion of their atmospheric flight. The left panel displays the histogram of each phenomenon; the right panel shows how the observational occurrence rate of MRAs/PTs varies as a function of velocity. The "MRA" data in each plot includes all MRA events, that is, those which had only an MRA (no PT) *and* those which had both an MRA and a PT. The same conditions apply to the "PT" data. Using the calculation detailed in Section 4.4, we determined representative 95% confidence intervals in the occurrence rate by assuming that the number of events with MRAs and/or PTs within each velocity interval follows a Poisson process. Both panels of Figure 6 were binned into 5 km/s intervals for easy readability. Examination of the different occurrence rates reveals several interesting trends. For starters, PTs are typically produced by slower meteors—this behavior is expected based on Cordonnier et al. (2024). On the other hand, MRAs exhibit the opposite trend: faster meteors are more conducive for MRA formation, either by virtue of the velocity itself or quantities which are strongly correlated with velocity. This too agrees with previous literature, which found the majority of MRAs arising from meteors faster than 45 km/s (Obenberger, Holmes, et al., 2016; Varghese et al., 2021). Under the present binning schema, a velocity of ∼35 km/s demarcates the boundary between PT-dominated and MRA-dominated regimes.

The distribution of events having both MRAs and PTs is perhaps the most enlightening aspect of Figure 6. Above velocities of ∼50 km/s, the majority of PTs also exhibited an MRA: out of the 27 "fast" PTs, 21 (78%) had an MRA. A similar, albeit weaker, trend is also seen at low velocities ($v < 25$ km/s), with 26 of the 42 MRAs (62%) in this range also having a PT. Both of these observed rates exceed the expected rates by more than a factor of 2, that is, the overall MRA occurrence rate above velocities of 50 km/s is only 30% and the PT occurrence rate below 25 km/s is only 22%. This suggests that there is indeed a connection between the two phenomena, augmented at the velocity extrema, such that observation of the non-dominant phenomenon (with respect to the given velocity regime) increases the likelihood that the dominant phenomenon is also present. For instance, an MRA produced by a very slow-moving meteor has an increased chance of also forming a PT (relative to the typical PT occurrence rate); the situation is reversed when a fast-moving meteor leaves behind a PT.

We note that the data shown in Figure 6 and the resulting analyses are purely observational; they make no attempt at normalization. Here, we will address two potential normalization schemes and their consequences. The optical meteors used in the directed MRA search were originally observed by brightness-limited instruments (i.e., the cameras of the GMN)—this introduces a lower mass limit which varies with velocity. Slow meteors will have a increased lower mass limit relative to their faster counterparts. We find that meteoroids more massive than $\sim 10^{-4}$ kg are detectable across the full range of velocities. Consideration of only this subset of meteors reveals the same excesses indicated above, with the observed rates exceeding the expected rates by a factor of at least 1.5 in the velocity extrema (i.e., faster than 50 km/s or slower than 25 km/s). We can also normalize based on altitude, and only include events which exist at a favorable altitude for both phenomena. That is to say, the meteor ought to begin above 86 km (MRA condition) and end below 93.5 km (PT condition); meteors satisfying these conditions have the potential to produce either phenomenon. With this restriction, the observed rates still exceed the expected rates by at least a factor of 1.7 in the velocity extrema. As this trend still appears under these normalization strategies, we are inclined to believe that it is physical in nature. The cause of this curious behavior is presently unknown, though its interpretation will likely first require a better understanding of the MRA emission mechanism.

To validate that the overall co-occurrence of PTs and MRAs is quantitatively significant, we performed a χ^2 test of independence. Of the 2,887 meteors under consideration: 544 showed only MRAs, 241 had only PTs, 131 had both an MRA and PT, and the remaining 1971 had neither. The test indicates that there is a significant relationship between PTs and MRAs, $\chi^2(1, N = 2887) = 33.38, p < 0.001$. That is to say, PTs and MRAs are co-produced more frequently than would be expected if they were completely independent processes. Despite this relationship, the fact that the number of events having only MRAs is 4 times larger than the number which also had PTs implies that MRAs are not as reliant on the PT mechanism as had been previously suggested in Obenberger et al. (2020).

4.6. Dynamical Origin and Strength

Cordonnier et al. (2024) found that a meteoroid's dynamical origin, traced by the Tisserand parameter with respect to Jupiter (T_J), and a meteoroid's mechanical strength, traced by the K_B parameter, were both important factors for the formation of PTs. We now repeat this investigation using MRA meteors to see if any comparable dependencies exist. The Tisserand parameter remains roughly invariant following gravitational perturbations by a massive body, for example, Jupiter; it is therefore broadly reflective of the true dynamical origin of a meteor's parent object (and by extension, of the meteor) regardless of the object's current, potentially modified orbit. When calculated with respect to Jupiter, it has the following form:

$$T_J = \left(\frac{a_J}{a}\right) + 2\sqrt{\left(\frac{a}{a_J}\right)(1 - e^2)}\cos i \tag{4}$$

where a, e, and i are the meteoroid's semimajor axis, eccentricity, and inclination (respectively), and a_J is the semimajor axis of Jupiter. This equation is derived from a restricted three-body problem, which implicitly assumes that only Jupiter perturbs the meteoroids and which neglects the effects of non-gravitational forces. The value of T_J can be used to generally associate an object with a particular class of orbits and origins: objects with $T_J \leq 2$ are on orbits consistent with nearly isotropic comets (NICs), originating in the Oort cloud, those with $2 < T_J \leq 3$ correspond to Jupiter family comet (JFC) orbits, originating from the Kuiper belt, and those with $T_J > 3$ have astroidal orbits, from the main asteroid belt. These are the typical categorical boundary limits used, however

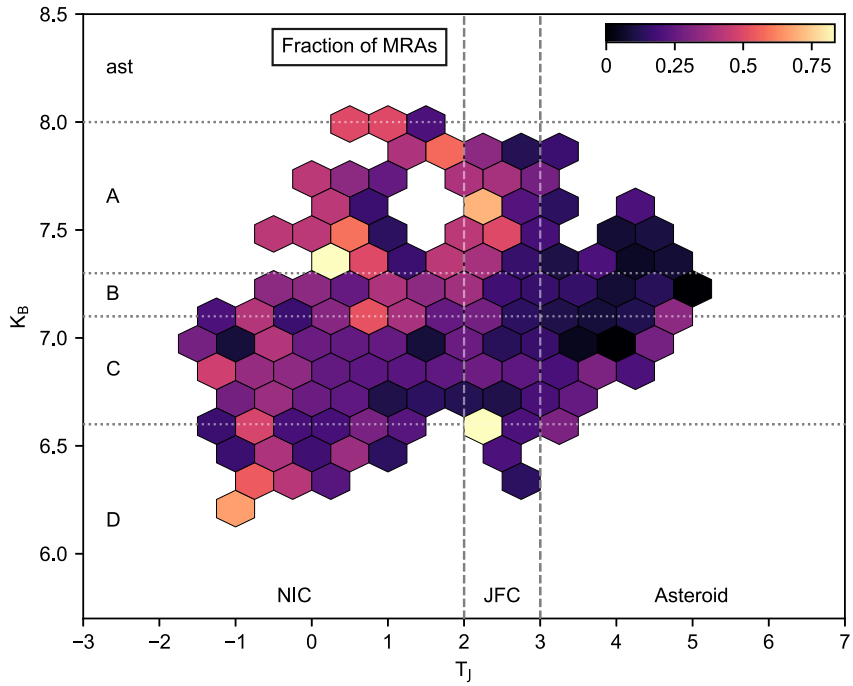

Figure 7. Heat map for the fraction of meteors beginning above 86 km that left MRAs, as a function of K_B and T_J. The boundaries between the different Ceplecha types and dynamical classes are indicated. Only cells containing at least five meteors are shown. There does not appear to be any strong clustering or preferred values among these MRAs.

they are not rigid and are occasionally adjusted slightly to better reflect observations (Jewitt et al., 2015), and there are a few known exceptions which defy this classification scheme. The K_B parameter, on the other hand, was initially developed by Ceplecha (1958) as a means to determine normalized meteoroid strengths, accounting for velocity, entry angle, and atmospheric density. We calculated this parameter according to:

$$K_B = \log \rho_B + 2.5 \log v_\infty - 0.5 \log \cos z_R - 0.10 \quad (5)$$

where ρ_B is the atmospheric density (g cm^{-3}) at the onset of ablation, v_∞ is the pre-atmospheric velocity (cm s^{-1}) of the meteor, and z_R is the zenith angle of the radiant (Ceplecha, 1958). Atmospheric density values were estimated using the MSIS 2.1 model (Emmert et al., 2022). The constant −0.10 term was empirically derived (Cordonnier et al., 2024) and accounts for the sensitivity difference between Ceplecha's original Super-Schmidt cameras and the GMN cameras. Ceplecha (1988) later divided K_B values into five general classes, each of which is associated with a particular composition. In order of decreasing meteoroid strength, these classes are: asteroidal ordinary chondrites ($K_B \geq 8$), group A carbonaceous chondrites ($7.3 \leq K_B < 8$), group B dense cometary material ($7.1 \leq K_B < 7.3$), group C regular cometary material ($6.6 \leq K_B < 7.1$), and group D soft cometary material ($K_B < 6.6$). Much like T_J, these are best thought of as rule of thumb classifications rather than absolute boundaries.

Figure 7 depicts the fraction of meteors which had MRAs, plotted within the K_B and T_J parameter space. It has been altitudinally normalized such that only meteors beginning above 86 km (i.e., those in the MRA zone) have been included. Furthermore, hexes are only shown if the binned data included at least 5 meteors; this reduces the effects of small number statistics on the resulting visualization. Unlike PTs which exhibited clear clustering when K_B was plotted against T_J (Cordonnier et al., 2024), MRAs show no strong preference within this parameter space. In general, asteroidal orbits are least favorable for MRAs, with only 93 out of 603 (15%) altitude-filtered meteors leaving them behind, though this behavior is not entirely unexpected. Meteors on these asteroidal orbits typically have velocities less than ∼40 km/s which, as per the previous section, are not particularly fruitful for MRA production. For comparison, 23% of meteors on JFC orbits left behind MRAs and 30% of those on NIC orbits did the same. At this stage, it is uncertain whether this trend arises by dint of the velocity itself, or if the

dynamical origin and composition actually play a significant role. In regard to K_B, there is no obvious preference for any particular class or strength of material. However, we performed a two-sample KS test comparing the K_B values of meteors with MRAs and those without (only considering those beginning above 86 km), which suggested that these distributions are different (p-value: 0.02). The distribution of MRA events is peaked at slightly lower (i.e., weaker) K_B values compared to those without MRAs, though these MRA events also appear to have slight excesses at both K_B extrema—that is to say, the K_B distribution of meteors with MRAs is slightly broader compared to those without. Unlike PTs which preferentially favor weaker material, the strength of the meteoroid's material appears to not play a substantial role in determining the likelihood of producing an MRA.

4.7. Meteor Showers and Sporadics

A detailed examination of MRA occurrence across different meteor showers has not previously been reported. Obenberger, Dowell, et al. (2016) found an increased number of MRA events coincident with known meteor showers, such as the η-Aquarids, Perseids, and Orionids, however they did not explicitly associate their 124 MRAs with meteors in these showers or perform normalization based on meteor counts. Varghese et al. (2021) examined 28 MRAs which were co-observed optically by the GMN, and found 15 associated with showers (including 8 from the Perseids) and the remaining 13 from sporadic meteors. Observations made during the peak of the 2020 Perseids were performed by Dijkema et al. (2021) using the LOFAR radio telescope, during which time they observed 204 radio trails with an optical meteor counterpart. They state that their all-sky imaging typically failed for frequency subbands containing strong meteor reflections from terrestrial sources (with those data being removed), however it is unclear from their data reduction pipeline what steps were taken, if any, to mitigate RFI/meteor reflection in cases where the imaging did not fail (e.g., filtering based on polarization fraction) before they averaged across all their subbands. Accordingly, we cannot assume that all 204 detected events would be classified as a bona fide MRA under the schema outlined in the present work. Additional observations made during the 2020 Geminids and 2021 Quadrantids resulted in "significantly fewer" MRAs relative to their Perseid meteor shower campaign (Dijkema et al., 2021).

Table 1 shows the meteor/MRA counts for the subset of meteor showers which had at least 10 meteors; the complete data set, including the less populated showers, can be accessed from the Open Research section. Table 1 includes a column indicating the number of MRA events which also had an observable PT, to facilitate identification of showers likely to produce both phenomena. The column indicating the occurrence rate of MRAs was computed relative to the number of meteors which began above 86 km, in order to provide a roughly normalized rate which only considers events which had the capacity to form MRAs (i.e., those which existed at favorable altitudes). We reiterate here that our present campaign only includes meteors which occurred during nighttime, moonless conditions, in accordance with the optical observation strategy. If daytime atmospheric conditions interact with meteors in a substantially different way, then our reported data will likely not be in agreement with results derived from such continuous, 24-hr observations. The data indicate no strong preference between shower meteors and sporadics, with 26.1% of altitude-normalized sporadics producing MRAs and an aggregated 24.3% of meteors associated with showers doing the same. A few meteor showers in particular stand out as noteworthy in the context of the aforementioned literature. We detected very few Perseid meteors which produced MRAs, only 2 out of the 17 observed meteors, which is substantially fewer Dijkema et al. (2021). This discrepancy can probably be attributed to the fact that our campaign only observed the 2022 Perseids, which peaked August 12/13 and coincided with a full moon on August 11. As the WiPT2 camera only operates during moonless conditions, the peak of the Perseid shower is not reflected in our MRA data; conversely, Dijkema et al. (2021) observed exclusively during the peak of the 2020 Perseids. Repetition of our analyses removing this lunar constraint should lead to an increased number of Perseid detections, consistent with Varghese et al. (2021) and Dijkema et al. (2021). Our findings agree with a low MRA occurrence rate for Geminid meteors, with only about 10% producing MRAs; however, 8 of the 16 MRA events also exhibited PTs. This is potentially related to the average velocity of the Geminids (~35 km/s) which occurs near the transition regime between PT and MRA dominance (as shown in Figure 6) Unexpectedly, we found the Quadrantids to be particularly fruitful for MRAs, having the one of the highest, non-trivial occurrence rates at 53.3%. Of the 30 observed Quadrantid meteors, 26 were associated with the 2022 shower (13 MRAs) and 4 with the 2023 shower (3 MRAs). The moderate average velocity of this shower, 41.1 km/s, would not traditionally be expected to produce such a large fraction of radio events. On the other hand, the high velocity Orionids ($v_{avg} = 65.2$ km/s) had a relatively weak showing with only 16.1% of meteors producing MRAs.

Table 1
MRA Production by Meteor Shower[a]

Shower name	IAU code	v_{avg} (km/s)	Total meteors	Meteors above 86 km	MRAs	MRAs with PTs	%MRA
Sporadic	…	41.1	1659	1454	379	61	26.1
Geminids	GEM	34.8	167	167	16	8	9.6
Orionids	ORI	65.2	112	112	18	0	16.1
Southern Taurids	STA	28.8	69	67	6	4	9.0
σ-Hydrids	HYD	59.0	44	44	19	6	43.2
Comae Berenicids	COM	63.0	42	42	10	1	23.8
April Lyrids	LYR	47.6	41	41	13	2	31.7
Leonids	LEO	69.2	36	36	11	0	30.6
Northern Taurids	NTA	29.9	31	29	5	3	17.2
Quadrantids	QUA	41.1	30	30	16	4	53.3
s-Taurids	STS	30.7	26	26	6	3	23.1
ν-Eridanids	NUE	65.8	21	21	8	1	38.1
Andromedids	AND	18.8	20	20	2	1	10.0
November Orionids	NOO	42.9	18	18	3	0	16.7
δ-Arietids	DAT	30.7	18	18	5	2	27.8
o-Eridanids	OER	29.7	17	17	5	2	29.4
Perseids	PER	57.8	17	17	2	0	11.8
Southern δ-Aquariids	SDA	41.2	16	16	7	1	43.8
f-Taurids	FTR	29.1	14	14	1	1	7.1
η-Aquariids	ETA	66.3	14	14	7	0	50.0
December Monocerotids	MON	41.9	13	13	5	2	38.5
Southern χ-Orionids	ORS	30.3	12	10	1	1	10.0
τ-Arietids	TAR	30.2	12	12	2	2	16.7
π-Hydrids	PIH	69.9	11	11	5	0	45.5
Ursids	URS	34.7	11	11	4	1	36.4
η-Corvids	ECV	67.4	10	10	1	0	10.0
τ-Taurids	TAT	28.4	10	10	2	1	20.0
τ-Cancrids	TCA	67.0	10	10	4	0	40.0

[a]Columns include the average velocity of the shower (v_{avg}), the total count of observed meteors, the count of meteors that began above 86 km (i.e., those in the MRA zone), the number of MRAs, the number of MRAs which also exhibited PTs, and the percentage of meteors that left an MRA (relative to the those in the MRA zone).

Figure 8 shows the relationship between the average velocity and MRA occurrence rate for those meteor showers having more than 20 total meteors, according to the data in Table 1. The velocity value for each shower was computed by finding the mean of the constituent meteors' average velocities. The indicated 95% confidence intervals for the occurrence rate were calculated in the same manner as in Section 4.4 for each shower. There is a discernible correlation between velocity and MRA production among the depicted showers, with a Pearson correlation coefficient of 0.47 (p-value: 0.12). However, there are some peculiarities present, such as the outsized MRA rate of the Quadrantids or the fact that the occurrence rate among the Orionids is similar to showers with velocities less than 35 km/s. These considerations suggest that factors beyond a simple velocity dependence are important for determining whether an MRA is likely to form.

4.8. Gradient Boosting Classification

In order to determine which meteor parameters are most relevant for the formation of MRAs, we subjected our data to a gradient boosting classification (GBC) algorithm (Friedman, 2001) in an attempt to differentiate between meteors which had MRAs and those which did not. We selected 20 meteor parameters from the GMN data set,

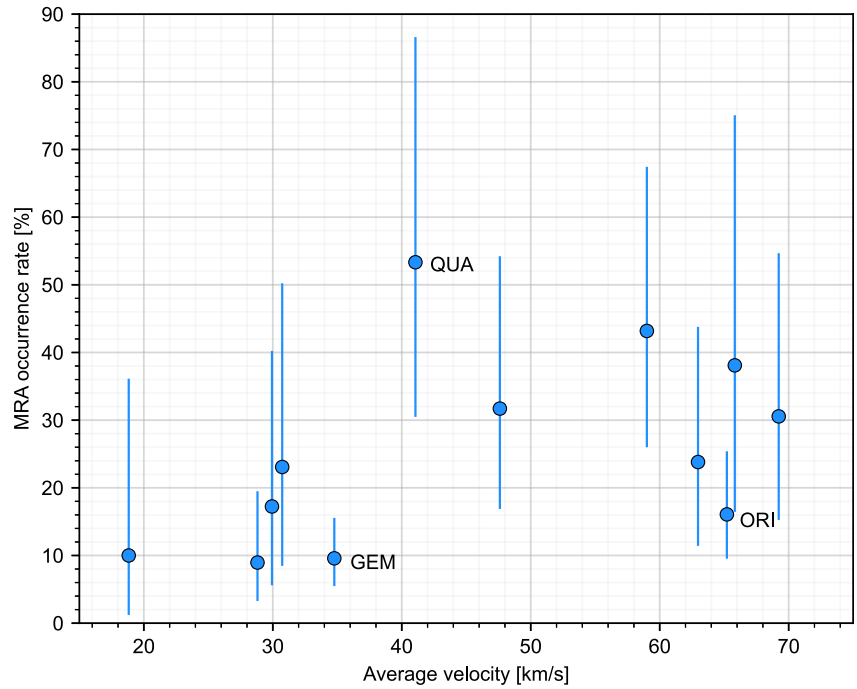

Figure 8. MRA occurrence rates for meteor showers having more than 20 total meteors, as a function of the showers' average velocity. Occurrence rates have been calculated with respect to the number of meteors beginning above 86 km. Error bars indicate the 95% confidence interval in the occurrence rate for each shower (see text). Several meteor showers have been explicitly labeled: the Geminids (GEM), the Quadrantids (QUA), and the Orionids (ORI). An overall positive correlation exists between these two quantities.

along with the derived K_B parameter, for a total of 21 features (listed in Table 2). These features are meant to reflect intrinsic meteor properties, and as such do not contain data relating to factors such as time or sky/ground positioning. Additionally, strongly correlated pairs were reduced to a single representative quantity; for example, the initial ground-fixed velocity of a meteor is strongly correlated with the average ground-fixed velocity, therefore only one of these was included (the average velocity). This helps to mitigate the splitting of significance between closely related quantities. The gradient boosting framework was implemented using scikit-learn (Pedregosa et al., 2011). We utilized StratifiedShuffleSplit in order to generate 100 independent model runs, where each iteration was divided into the typical 80–20 train/test split. The compute_sample_weight function was used to mitigate the class imbalance between the two meteor classes during model training, which it accomplished by weighting based on the relative frequency of each class within the training data set. The hyperparameters of the GBC model itself were optimized using a grid search technique with cross-validation (GridSearchCV); the tuned model was then fit to the training data for each of the 100 iterations. The overall accuracy of each classification was calculated using the respective test dataset—across all iterations, its mean value (and standard deviation) was $82.0 \pm 1.3\%$. That is to say, if the 21 parameters listed in Table 2 for a given meteor were input into the trained GBC model, it would correctly predict the presence (or absence) of an MRA 82% of the time.

The relative feature importances were also determined for each run; the averaged values are reported in Table 2. Because the training data is randomly selected during each instance of the GBC, we opted to use the average feature importance across many (100) trials in order to better represent each parameter's importance. Likewise, we calculated the standard deviation across these 100 trials for each feature's importance, as a way to measure of the "stability" of that feature. This value is also reported in Table 2. Surprisingly, we find that a meteor's entry angle dominates the decision tree, accounting for 31.5% of the total importance—this strong dependence has not been identified in previous literature and will be investigated further in Section 4.9. The remaining important features are more or less expected, including the altitude at which the meteor begins and ends, the peak optical brightness and the mass of the meteor, the duration of the meteor, and its average velocity. These parameters are not entirely independent; for example, a meteor's (photometric) mass is derived from its brightness, slower meteors tend to have longer durations, and the three altitude statistics (beginning, peak, and end heights) are closely related. The

Table 2
Feature Importance From Gradient Boosting Classifier[a]

GMN variable	Description	Importance [%]	σ [%]
Elev	Entry angle	31.53	1.05
HtBeg	Meteor begin height	7.62	0.87
Peak	Peak absolute magnitude	6.41	0.65
HtEnd	Meteor end height	6.41	0.58
Mass kg	Meteor mass	5.59	0.64
Peak Ht	Height of peak meteor brightness	4.92	0.64
Duration	Observed meteor duration	4.64	0.70
Vavg	Apparent average velocity	4.16	0.62
e	Eccentricity	2.91	0.44
node	Ascending node	2.74	0.32
i	Inclination	2.67	0.38
b	Latitude of perihelion	2.63	0.35
KB	K_B parameter	2.42	0.34
F	F parameter	2.24	0.26
TisserandJ	Tisserand parameter w.r.t. Jupiter	2.10	0.39
q	Perihelion distance	2.05	0.27
n	Mean motion of the orbit	2.02	0.32
Pi	Longitude of perihelion	1.98	0.25
a	Semi-major axis	1.74	0.27
f	True anomaly at meteor beginning	1.73	0.24
peri	Argument of perihelion	1.50	0.19

[a]The Importance column provides the average relative feature importance across 100 trials (column sums to 100%). The σ column indicates the standard deviation of the associated feature's importance across the 100 trials.

high relative importance of the altitudinal quantities is quite natural, as MRAs are known to have an altitudinal cutoff (Obenberger, Holmes, et al., 2016). MRA meteors have a slight preference for higher masses relative to the non-MRA meteor sample, with median values of 0.18 and 0.13 g, respectively; this is equivalently seen as MRAs slightly favoring brighter meteors. The origin of this difference might very well reflect a physical mass cutoff, though it could just as easily result from the intrinsic sensitivity threshold of the LWA instrument. Generally, the meteoroid's orbital parameters appear to have little influence in MRA formation.

We attempted to repeat this GBC schema utilizing all four possible meteor classes: MRA only, PT only, both MRA and PT, and neither phenomenon. The data were labeled accordingly and were processed via the same pipeline as described above, using the same 21 features and a GBC model with retuned hyperparameters. Again, 100 independent model runs were carried out and the resulting statistics were aggregated across all runs. When applied to the test data, the overall accuracy had a mean value of only 67.8 ± 8.4%, which is substantially worse than the previous classification scenario; the large variation also indicates that the resulting GBC models are not particularly stable. This suggests that a wholistic approach to distinguishing between all four classes is largely intractable using this technique, with the classes overlapping too much for clean separation. In spite of this, the two most important features were found to be meteor end height (10.8 ± 1.7% relative importance) and entry angle (9.5 ± 2.0% relative importance). These features align with expectations, as entry angle is of primary interest to MRAs (based on Table 2) and ending height is the most relevant feature for PTs (based on Cordonnier et al., 2024).

4.9. Entry Angle

Figure 9 compares the distribution of entry angles for meteors which had MRAs and those which did not; an entry angle of 0° is parallel to Earth's surface whereas 90° is perpendicular. There is a stark difference between these two samples, with MRA meteors strongly preferring shallow entry angles. The median entry angle for the non-MRA sample is 55.1°. MRA meteors, on the other hand, have a median value of only 35.7°; their 90th percentile value is 53.4°, which is still less than the median of the non-MRA sample. Though the behavior was not explicitly identified, the entry angles of the 31 MRAs depicted in Varghese et al. (2021) are also seen to preferentially favor shallower angles. We performed a two-sample KS test between the entry angles of these 31 MRAs and of the 675 MRAs in our study; the result indicates that there is no significant difference between the two samples (p-value: 0.46). Though this test cannot prove that the samples were drawn from the same overall population, their similarity does help to corroborate the existence of this entry angle dependence.

The question naturally arises whether this dependence is due to a physical mechanism or instead results from geometric observational biases. We introduce two additional quantities here to aid in this interpretation: namely the meteors' projected angular sizes and their perspective angles. The projected angular size of a meteor is readily calculated from GMN data by first converting the reported geodetic beginning and end coordinates into altitude/azimuth coordinates (relative to the LWA) and then finding the angular separation between these. Because MRAs exhibit an altitude cutoff, we only want to consider the projected angular size of the portion of the meteor within the MRA zone, assumed here to be 87 km and above. We computed the fraction of each meteor that existed above 87 km and multiplied this by the meteor's full angular size to estimate the projected angular size within the MRA zone. This angular size is an relevant consideration because the LWA telescope has a characteristic beam size at a given observing frequency. The synthesized half-power beamwidth (or "beam size") of an interferometric radio telescope depends on the wavelength (λ) of the observation and the diameter (D) of the array; it is roughly equal to $1.2 \times \lambda/D$ (in radians). At our reference frequency of 38 MHz ($\lambda = 7.9$ m), the beam size of the LWA ($D \approx 100$ m) is approximately 5.4°. Meteors which enter the atmosphere at shallower angles tend to have larger projected angular sizes on the sky relative to a fixed observer, meaning that they are more likely to fill an entire

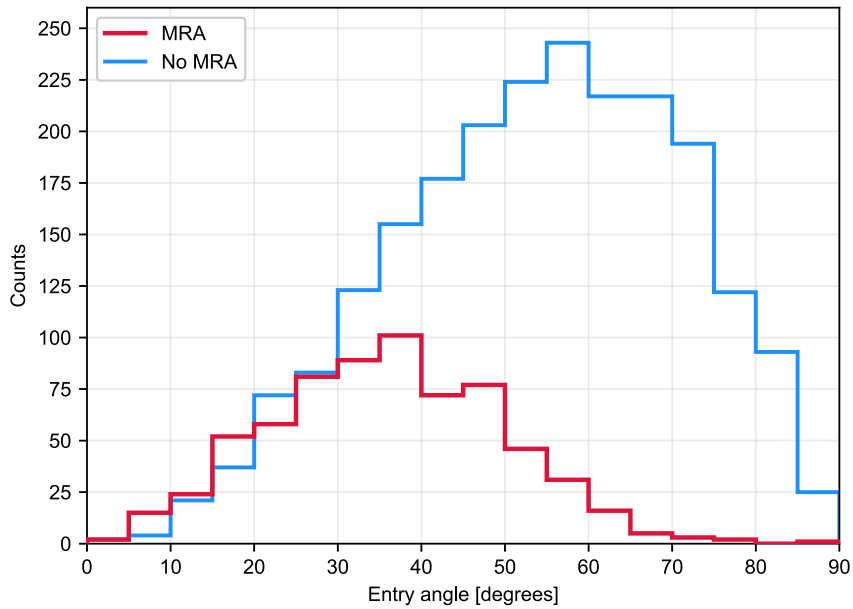

Figure 9. Histograms showing the number of meteors which had MRAs compared to those without MRAs as a function of entry angle. MRA meteors are much more prevalent at shallow entry angles, with only 4% of MRAs being produced by meteors entering the atmosphere at angles steeper than 60°.

LWA beam width—these would be theoretically easier to detect relative to a meteor with a projected angular size less than the beam size.

The left panel of Figure 10 shows the relationship between a meteor's entry angle and its projected angular size within the MRA zone. The right panel shows how this projected angular size affects the MRA occurrence rate, with the LWA beam size (at 38 MHz) being shown for both plots. The occurrence rate was computed per 7°

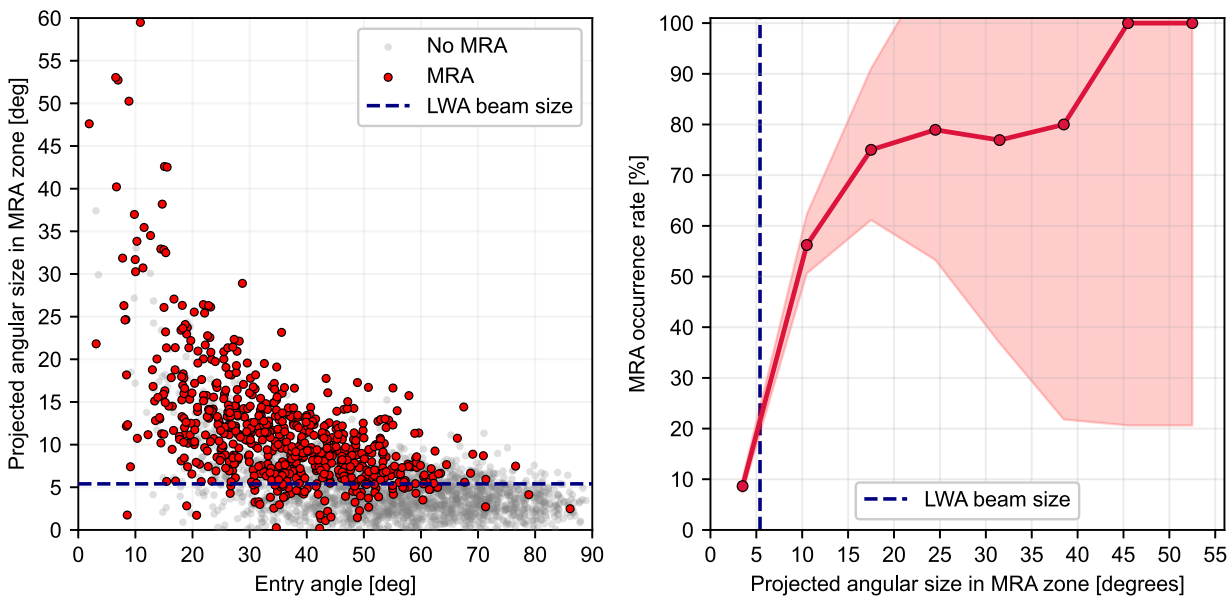

Figure 10. (left) The relationship between a meteor's entry angle and its projected angular size for the portion of its trajectory above 87 km (taken to be the "MRA zone"). Gray dots indicate the meteors which did not have MRAs, while red dots show those that did. The blue dashed line indicates the size of the LWA's beam at a frequency of 38 MHz (5.4°); events above this line are considered "beam-filling." (right) MRA occurrence rate as a function of the projected angular size (binned into 7° intervals). The shaded region shows the 95% confidence interval for each point (computed according to Section 4.4). The large confidence intervals are a direct consequence of small number statistics. The LWA beam size is included for reference; below this size scale, the MRA detection rate is very low.

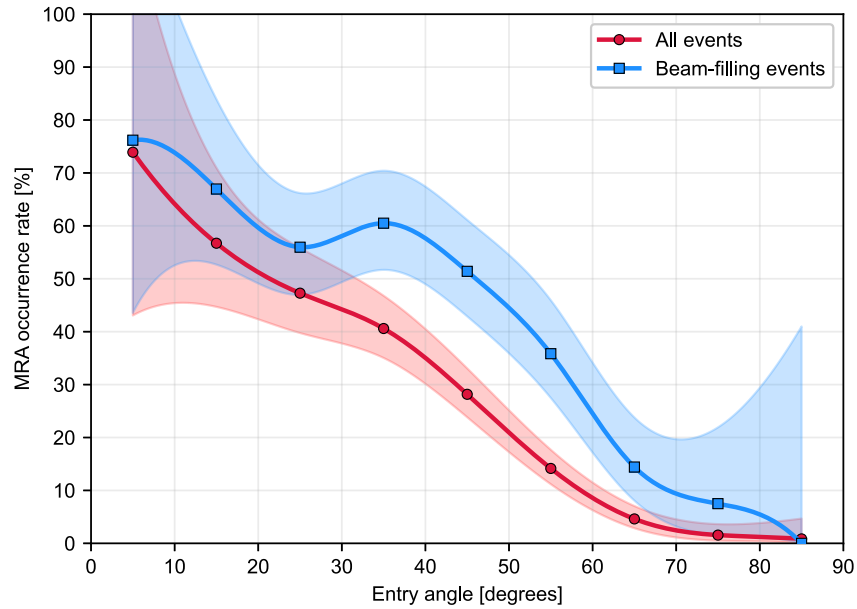

Figure 11. MRA occurrence rate as a function of meteor entry angle (binned into 10° intervals). The red curve depicts the occurrence rate as calculated using all meteors observed in the campaign, without applying any filtering. The blue curve repeats this calculation but includes only the beam-filling meteors, that is, meteors with projected angular sizes in the MRA zone which exceed the LWA beam size at 38 MHz (about 5.4°). The shaded regions show the 95% confidence interval for each point (computed according to Section 4.4); data points and confidence intervals have been smoothly connected via cubic interpolation.

angular size bin, with the associated 95% confidence intervals being computed in the same manner as in Section 4.4; the sizable confidence intervals at large angular scales are a direct consequence of the small number of meteors with observed values in those ranges. The MRA occurrence rate follows the expected trend, such that small projected angular sizes are vastly less conducive for detecting MRAs. Projected angular size is accordingly a major source of observational bias. However, the left panel suggests that the relationship between projected angular size and entry angle is more complex than a naive sensitivity argument would suggest. If geometry (as traced by the projected size) was the primary driver of the entry angle dependence, then there ought to be a particular cutoff size below which MRAs are not detected—across all entry angles. In reality, the population of MRAs which occur below the beam size threshold (i.e., the non-beam-filling events) are skewed towards lower entry angles, despite the fact that the overall meteor population favors larger entry angles in this regime. In other words, even below the angular size cutoff there is a much higher MRA rate at low entry angles than at high entry angles: 10.4% of meteors with entry angles shallower than 55° had MRAs, compared to a rate of only 1.7% at angles steeper than this. If we instead look at the inverse population, that is, the "beam-filling" meteors (with angular sizes in the MRA zone larger than 5.4°), then we find that the entry angle dependence still persists. This is shown in Figure 11, which compares the MRA occurrence rate as a function of entry angle for all events (without filtering) and for just the beam-filling events.

Normalizing by the beam size is not a perfect technique however, since there is no guarantee that the true MRA emission region actually fills the entire beam; it does restrict the data to only those cases where an MRA has the potential to fill it though. Likewise, the 87 km altitude cutoff used to determine the projected angular size is not a hard boundary, but is rather an empirical, approximate one (based on the information presented in Section 4.1). Under these assumptions, the data do appear to suggest that a meteor's projected angular size cannot entirely explain the observed entry angle dependence. We do not, however, discount the possibility that a more rigorous approach (e.g., using the solid angle subtended by a meteor, or only including resolved MRAs) would ultimately reveal the antithetical position.

The perspective angle θ_p characterizes the direction of the meteor with respect to the line of sight from the observer; mathematically, it is obtained from a simple dot product and can be defined as:

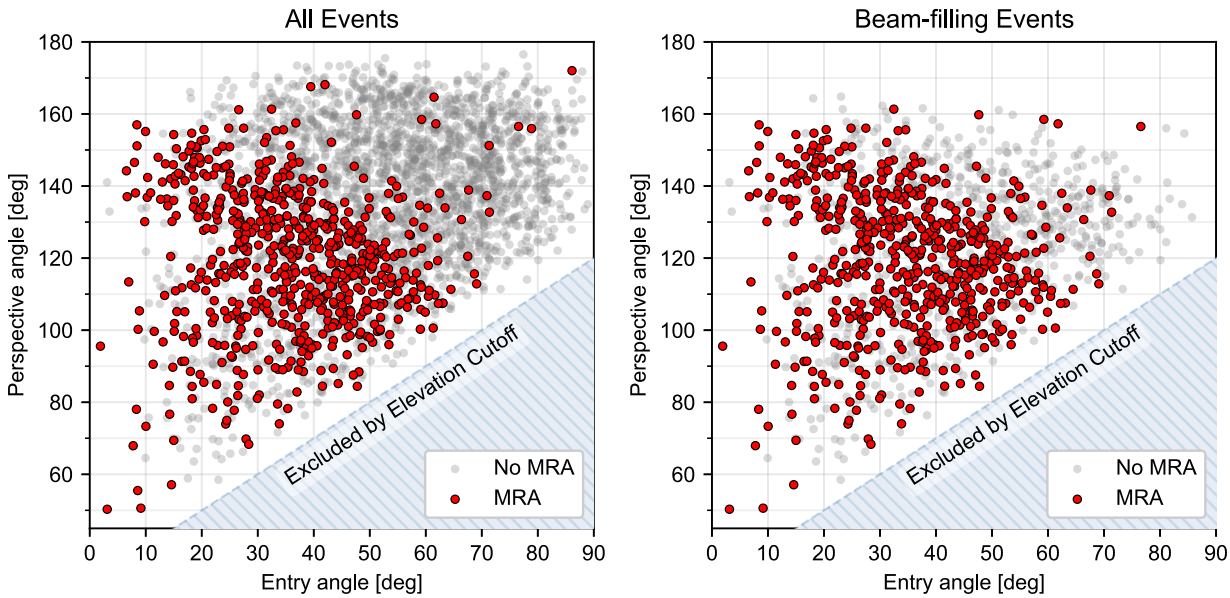

Figure 12. (left) The relationship between a meteor's entry angle and its perspective angle. Gray dots indicate the meteors which did not have MRAs, while red dots show those that did. The shaded region is excluded because our 30° elevation cutoff renders certain perspective angles unattainable for a given entry angle. The majority of the MRA population appears to be contained below a diagonal boundary line in this parameter space. (right) Same as previous, though this panel only includes events with projected angular sizes greater than 5.4° in the MRA zone (i.e., the beam-filling events).

$$\theta_p = \arccos(\hat{\mathbf{r}} \cdot \hat{\mathbf{m}}) \tag{6}$$

where $\hat{\mathbf{r}}$ is the unit vector pointing from the observer to the start point of the meteor and $\hat{\mathbf{m}}$ is the unit vector pointing from the meteor's start point to its end point. Accordingly, a perspective angle of 180° means the meteor is headed directly towards the observer, $\theta_p = 90°$ appears broadside to the observer, and $\theta_p = 0°$ would be originating from the observer towards space (and is therefore unphysical). In performing this calculation, the geodetic coordinates of the LWA station and the meteors' start/end points were first converted to ECEF coordinates for simplicity. This perspective angle is not entirely disconnected from the projected angular size, for example, meteors with high perspective angles (the "head-on" trajectories) will tend to have very small projected sizes. Figure 12 plots entry angle against perspective angle for the total population of meteors and for just the subset satisfying the beam-filling criterion described above. A portion of the parameter space is excluded based on our observing strategy; since we only consider meteors at least 30° above the horizon, certain perspective angles are impossible to realize for a given entry angle. Perhaps the most striking feature seen in these plots is the obvious diagonal boundary beyond which MRA detections decline sharply. The majority of the non-MRA meteors in the high perspective angle, high entry angle regime (seen in the left panel of Figure 12) are associated with small projected angular sizes, as demonstrated by the reduction of this population upon making the beam-filling cut (right panel). However, the angular size argument does not entirely account for this non-MRA population. For example, consider an entry angle of 45°: based on the left panel of Figure 10, MRAs are detected across the entirety of the beam-filling sample, however the right panel of Figure 12 shows that there are a number of beam-filling events with high perspective angles which do not have MRAs. In other words, perspective angles larger a certain entry angle dependent threshold appear to be unfavorable for detecting MRAs, even when only considering those events which have sufficiently large projected angular size. Interestingly, though perhaps coincidentally, the diagonal cutoff boundary in Figure 12 is roughly defined such that the sum of perspective and entry angles is 180° (e.g., an entry angle of 45° has an MRA detection boundary at perspective angles of ∼130–135°). Work by Varghese et al. (2019) has indicated that MRAs emit isotropically, so it seems unlikely that the perspective angle dependence is related to directional MRA emission or beaming effects. Despite this, the data seem to imply that a meteor with a given entry angle has to be "aimed" in certain directions in order to have good detection efficiency, which suggests some sort of geometric consideration.

It is evident from the preceding discussion that the projected angular size, perspective angle, and entry angle influence one another in a complicated, intertwined fashion which requires careful and rigorous analysis beyond the scope of this paper. Furthermore, while it is presently difficult to ascertain whether the observed entry angle dependence is due solely to geometric biases or an underlying physical mechanism, this relationship would be straightforward to investigate in future work. Utilizing two or more LWA stations to observe the same MRAs (with meteors being parameterized by the GMN) would enable a rigorous comparative analysis which should ideally disentangle the effects of geometry and/or intrinsic physics. In light of this, it is perhaps most prudent to leave the final interpretation of this topic to such future analyses.

5. Conclusions

In this work, we have expanded the meteor/PT catalog of Cordonnier et al. (2024) to include MRA classification and associated parameters. This was accomplished using all-sky radio observations made by the Orville Wide-band Imager system at the LWA-SV telescope. The present catalog included a total 2887 meteors, of which 675 had MRAs and 372 produced PTs; this large sample of events enabled meaningful statistical analyses to be performed. We were particularly interested in investigating the association between the MRA and PT phenomena, which was first observed and promulgated by Obenberger et al. (2020). Ultimately, a close relationship between these two phenomena was not borne out by our observations, though we did identify a statistically significant dependence between them. The main takeaways of this research can be summarized as follows:

1. The power law spectral index distribution for our sample of MRAs peaked at −2.92, which is consistent with previously reported values.
2. Under a log-normal spectral paradigm, the MRA turnover frequencies exhibit a weak negative correlation with MRA peak heights, as one would theoretically expect. Varghese et al. (2021) found the opposite trend, though this can be attributed to their small sample size and large correlation p-value.
3. The MRA occurrence rate did not show any strong temporal dependence over the 2 year campaign, unlike the strong semiannual variations exhibited by PTs. Though small-scale (∼monthly) oscillations and an overall decrease in the MRA rate can be discerned, the statistical uncertainty and potential instrumental bias prevent us from conclusively verifying these trends.
4. The transition between PT and MRA dominated regimes occurs at an average velocity of about 35 km/s, with MRAs preferring the higher velocities. Within the velocity extrema (faster than 50 km/s or slower than 25 km/s), the occurrence of the non-dominant phenomenon increases the likelihood of the dominant phenomenon by a factor of at least 1.5 relative to the normally expected rate. The mechanism responsible for this is presently unknown.
5. More than 80% of the MRAs observed in this work did not have an associated PT; this implies that MRA emission is not heavily reliant on the PT mechanism. However, we did find sufficient statistical evidence that these two phenomena are not wholly independent from one another.
6. In regard to dynamical origin, MRAs are more often produced by meteors on NIC orbits relative to asteroidal orbits; this dependence aligns with the expected velocity behavior and therefore cannot be definitively attributed to compositional differences. Meteoroid strength also appears to play no significant role in MRA formation.
7. We found that MRAs are produced by shower meteors and sporadic meteors at approximately the same rate. Though meteor showers with higher velocities tended to have higher MRA occurrence rates, notable exceptions were found. In particular, the Quadrantids had an unusually high MRA rate.
8. Using a gradient boosting classification algorithm, we obtained 82% accuracy in predicting whether a given meteor is likely to produce an MRA. Entry angle was found to be the most important feature for classification, with a meteor's altitudinal information (i.e., the beginning, peak, and end heights), brightness, mass, and duration also contributing to the overall importance.
9. Unexpectedly, MRA occurrence rates were found to heavily depend on a meteor's entry angle, with shallow angles producing high MRA rates. While clearly important from an observational standpoint, it is presently unclear whether this dependence ultimately arises from geometric biases or is rooted in some as yet undetermined physical process. Additional study using two or more LWA stations is expected to resolve this issue.

Future work would greatly benefit from a rigorous computational assessment (via modeling and simulation) of the proposed MRA emission mechanisms. While the results presented here (in conjunction with previous literature) can be used to inform such an evaluation, having a solid theoretical understanding of the MRA phenomenon is likewise crucial for both contextualizing and interpreting the observed data within the overall MRA production

framework. This is especially true of the relationship between PTs and MRAs, which as demonstrated here do not appear to have a straightforward correlation; understanding their complex interplay will necessitate a practical model of MRA formation. Additional observational data, especially pertaining to small-scale turbulent plasma structures and multi-station MRA co-detections, will ideally place constraints on the potential MRA emission mechanisms and resolve the questions associated with the entry angle dependence.

Appendix A: Orville Astrometry

This Appendix describes the techniques and procedures used to improve the astrometric calibration of the Orville all-sky radio data. These images are nominally created using a slant orthographic projection, with an off-zenith phase center. However, attempting to reconstruct sky positions from image pixels using the astrometric parameters saved in each file results in an imperfect mapping with pointing errors that are approximately 0.6° on average. The cause of this discrepancy is being investigated in order to remedy future observations, however the existing archival data used in this work require a different, empirical approach. To this end, 60 Orville files were hand-selected from 6 days spread throughout the MRA observational campaign; these files were chosen such that they included bright radio sources during periods where both atmospheric and RFI environments were minimally intrusive, for both day and night times. The two frequency channels nearest to 38 MHz were averaged together to produce the overall images used in subsequent processing (this frequency range was accessible during both frequency epochs). For every frame, the pixel location of any bright radio sources (limited to Cyg A, Cas A, Vir A, and the Sun) was found by computing the centroid of a 2D Gaussian fit to the source; this step was facilitated by the photutils.centroids module (Bradley et al., 2024). These locations (and corresponding times) were then collated into a single large data set which served as the "true" pixel positions for the optimization stage. This data set contained a total of 63,670 pixel locations, the majority (85%) of which were associated with Cyg A and Cas A. Owing to its large angular size and variability, the Sun is a less than ideal source to use for precision astrometry, however it is one of the few bright radio sources in the southern direction—it was therefore included to prevent overfitting northerly positions (viz. Cyg A and Cas A) to the detriment of those toward the south.

We utilized Astropy's World Coordinate System (WCS) to handle the transformation between pixel and celestial coordinates and vice versa. Owing to its computational efficiency, our WCS was constructed using an hour angle (HA) and declination (Dec) equatorial coordinate system—this meant that a single WCS object could be applied to all observations. This is because the association between HA and any given pixel is essentially invariant much like the altitude/azimuth system, whereas right ascension (RA) values do not remain static over each pixel. HA can easily be converted into RA using the local sidereal time (LST) according to: $RA = LST - HA$. The WCS object was constructed with the following parameters left as variables to be optimized: CRVAL1 (HA of reference pixel), CRVAL2 (Dec of reference pixel), PV2_1 (ξ), PV2_2 (η), and LONPOLE (see Calabretta and Greisen (2002) for a complete description of these keywords). The ξ and η parameters control how much the slanted projection is "stretched" relative to a standard orthographic projection. Minimizing the root mean square value of the differences between sources' actual pixel locations and the positions predicted by any given WCS model enabled the above parameters to be empirically optimized. This process was handled by SciPy's optimize.minimize function using the default L-BFGS-B solver (Zhu et al., 1997). Table A1 summarizes the results of this optimization and includes the other (non-optimized) parameters used in constructing the WCS.

Table A1
Parameters Defining the Optimized Orville Astrometry[a]

Parameter name	Keyword	Value	Unit
Projection type	CTYPE	"RA—SIN," "DEC–SIN"	
Reference pixel	CRPIX	64.5, 64.5	
Pixel scale	CDELT	1.015625, 1.015625	°
HA/Dec of reference pixel	CRVAL	357.38857, 33.50712	°
Slant parameter ξ	PV2_1	0.01183	
Slant parameter η	PV2_2	−0.00819	
Longitude of pole	LONPOLE	179.21441	°

[a]Values in the top 3 rows were assumed; values in the rest were optimized.

The improvement afforded by this optimization process can be visualized in Figure A1. The left histogram shows the distribution of angular offsets between the modeled and true source positions using the astrometric parameters contained in the Orville headers, and the right plot shows the same for the optimized astrometry. With the default header parameters, 9.8% of offsets were greater than 1° and 65.3% were greater than 0.5°. After optimization, 1.6% of offsets were greater than 1° and only 7.3% were greater than 0.5°. This new schema, therefore, represents a significant improvement in astrometric accuracy, especially when considering that the pixel scale is ∼1°/px near zenith.

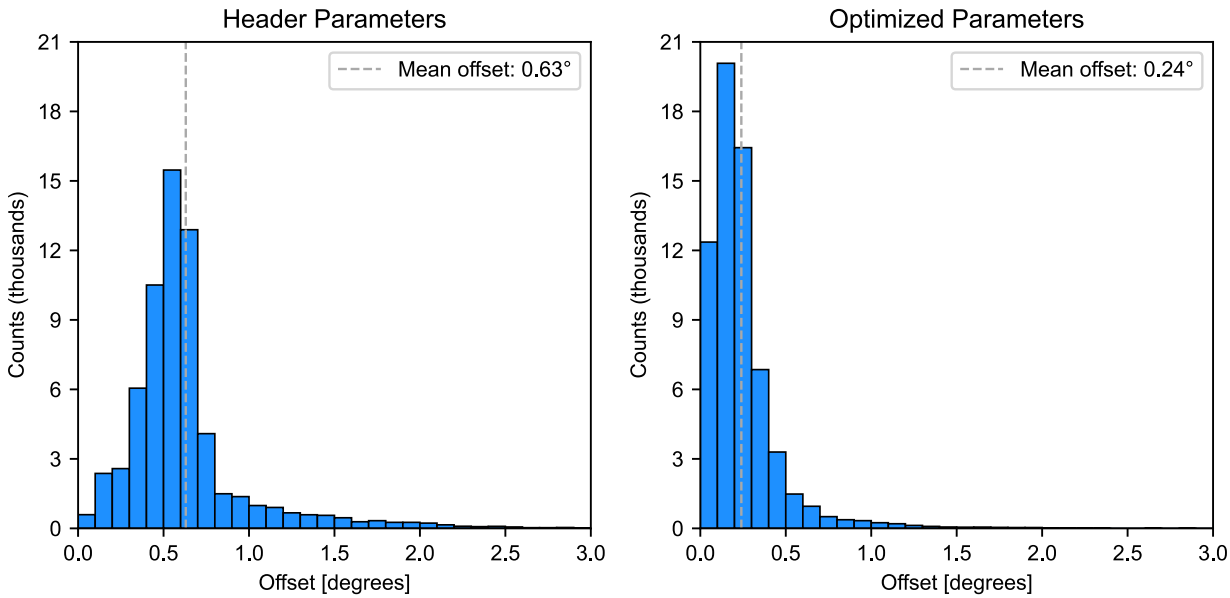

Figure A1. Histograms of angular offsets between the true source positions and those calculated by WCS using the default Orville header information (left) and the optimized parameters (right). The mean offset value for each is indicated by the dashed line.

Appendix B: Orville Flux Calibration

Flux calibration enables the arbitrary pixel values depicted in the Orville all-sky images to be converted into physically meaningful units. This process is initiated in the same manner as demonstrated in Varghese et al. (2019):

$$\frac{S_{\nu,CygA}[\mathrm{Jy}]}{P_{\nu,CygA}(elev)[\mathrm{a.u.}]} = \frac{S_{\nu,pix}[\mathrm{Jy}]}{P_{\nu,pix}(elev)[\mathrm{a.u.}]} \tag{B1}$$

where the flux density (S) in a particular frequency channel (ν) divided by the background-subtracted pixel value (P) at a given elevation angle ($elev$) is equivalent for some arbitrary pixel (pix) and calibrator source ($CygA$) at the same elevation. Flux density is measured in Janskys (Jy) and pixel values in arbitrary units (a.u.). Since the LWA's sensitivity varies as a function of elevation angle, it is important that the P values used in Equation B1 be measured at the same elevation.

The first step in solving Equation B1 therefore is to find $P_{\nu,CygA}(elev)$, i.e., how the pixel value of Cyg A changes in response to elevation angle. This needs to done not only for each of the 6 frequency channels, but also whenever the sensitivity of the instrument is changed (e.g., following a change in filter/attenuation settings). There were 10 such major changes over the observing campaign, leading to the 10 separate sensitivity epochs shown in Figure B1. These can be broadly divided based on the analog filter settings into "undefined," "full," or "split" settings. The "undefined" status means that the filter information was not saved, as was the case during the first ∼125 days of our observing campaign. The "full" bandwidth setting has a uniform-gain response across the full 10–88 MHz operational range, while the "split" bandwidth setting employs a dual-gain scheme where frequencies below ∼35 MHz can be attenuated for RFI mitigation (Ellingson et al., 2013). Within each filter setting, subdivisions have been empirically delimited (1, 2, 3, etc.) based upon apparent changes in the behavior of the pixel value versus elevation profiles. We utilized the existing set of 1,487 Orville files as the basis for generating Figure B1, as these files depict the sky under the same atmospheric conditions that the MRAs experienced. A consequence of this, however, is that some of the shorter epochs (e.g., "split 2") only contain a narrow range of elevations, which require extrapolation techniques detailed further below. For each frame of each file, the sky was smoothed using a rolling median of 5 frames (2 before and 2 after the rolling frame) to minimize the impact of spurious frames due to RFI. These smoothed images were then fed into the Background2D class of the photutils. background Python package, which grids the image, sigma clips bright pixels, and then interpolates across bins as necessary in order to estimate the background sky (Bradley et al., 2024). These background images are free from

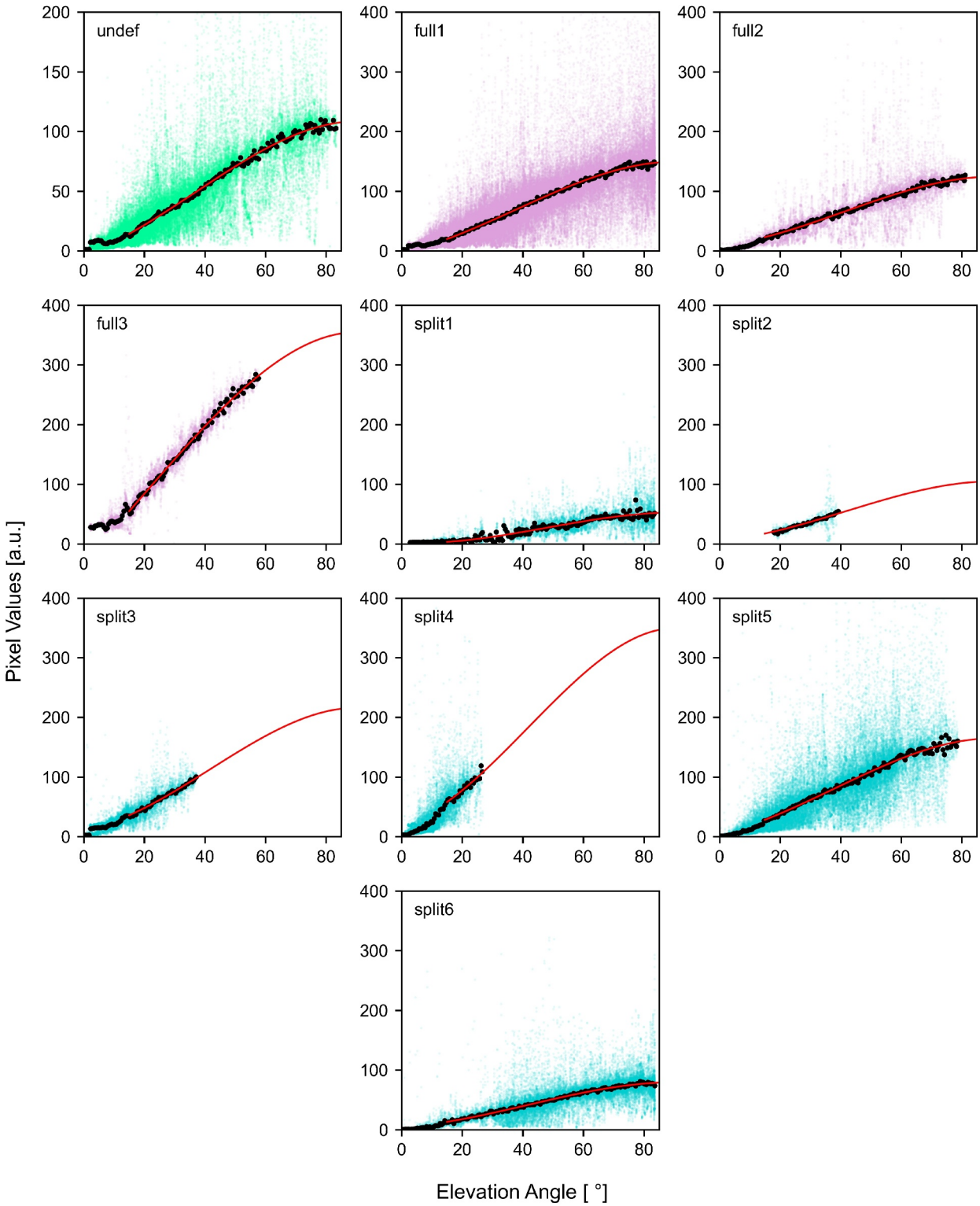

Figure B1. Pixel values of Cyg A as a function of elevation angle for each of the 10 Orville sensitivity epochs for frequency channel 5. Early data did not record the analog filter settings ("undefined"), but the remaining epochs used either "full" or "split" filters (defined in text) with numerals indicating subdivisions within each filter. The small colored dots depict individual measurements of Cyg A, with the larger black dots showing the median value per 0.5° elevation bin. The red curve reflects the fitted cubic equation. Split 6's line was rescaled to estimate split 2, 3, and 4.

point sources and are dominated instead by the diffuse galactic emission. After subtracting the background from each frame, the maximum pixel value and corresponding elevation of Cyg A were recorded; each colored point in Figure B1 represents one of these pairs. The median value for each 0.5° elevation bin was computed (shown as the black dots), which were then fit to a cubic polynomial (the red curve) constructed such that its maximum occurred at 90° elevation. Only elevations greater than 15° were used in the fit, as low elevations could be contaminated by RFI. The cubic equations for each filter's subdivisions are roughly constant scalings of one another. Because of this, the equations describing split 2, 3, and 4 were obtained by finding the best-fit scalar multiple of split 6's cubic equation. Split 6 was chosen as the template since it had the least variability relative to split 1 and 5. These 60 cubic equations (6 frequency channels across 10 epochs) enabled us to determine Cyg A's pixel value at any elevation angle, at any time, for any frequency—therefore completely describing $P_{\nu,CygA}(elev)$.

The spectral flux density of Cyg A was obtained from Baars et al. (1977), given as:

$$\log S_\nu = 4.695 + 0.085 \log \nu - 0.178 \log^2 \nu \tag{B2}$$

where S_ν is measured in Jy and ν in MHz. The midpoint of each frequency channel was inserted for ν above to get the corresponding reference flux density, $S_{\nu,CygA}$, used in Equation B1. The only quantity which remains to be specified in that equation, $P_{\nu,pix}(elev)$, is easily obtained from the background-subtracted images which are already produced in the MRA detection pipeline (see Section 3). The background-subtracted pixel of interest, in our context, is typically associated with the brightest pixel of an MRA. The elevation of this pixel can be determined using the optimized astrometry described in Appendix A, and the corresponding pixel value of Cyg A at that same elevation can be obtained from the appropriate cubic equation. In this manner, the flux density ($S_{\nu,pix}$) of any pixel in the image can be determined; repeating this process across all 6 frequency channels enables quantities such as the spectral index to be computed.

The statistical uncertainty in each calculated flux density was estimated according to the following equation adapted from Varghese et al. (2019):

$$\Delta S_{\nu,pix}[\mathrm{Jy}] = \left(\frac{S_{\nu,CygA}[\mathrm{Jy}]}{P_{\nu,CygA}(elev)[\mathrm{a.u.}]}\right) \sigma_{noise}[\mathrm{a.u.}] \tag{B3}$$

where $\Delta S_{\nu,pix}$ is the one-sigma uncertainty in the flux density and σ_{noise} is the standard deviation of the thermal noise intrinsic to each frequency epoch. For each frequency epoch (and each of the six frequency channels), the thermal noise was computed by first aggregating the individual background-subtracted meteor frames. From the resulting noise distributions, the standard deviation was estimated via its relationship with the MAD ($\sigma \approx 1.4826 \times MAD$ for normally distributed data). That is to say, we calculated the MAD and from that derived σ. This σ value is taken to be σ_{noise}. This approach was employed because the noise distributions exhibit large, non-Gaussian tails likely arising from the presence of scintillation (as no source masking was applied). These tails, therefore, are not representative of the intrinsic thermal noise and a direct computation of σ would be unnecessarily large. Using the MAD method results in σ values whose associated Gaussian profiles closely match the core of each noise distribution and are thus expected to better reflect the instrument's thermal noise. It is important to note that the uncertainties calculated above only account for the statistical contribution of noise; they do not include the effects of any systematic errors such as those caused by scintillation or terrestrial reflection.

Data Availability Statement

The catalog containing all meteors considered in this work, including the derived PT and MRA data, can be accessed at https://lda10g.alliance.unm.edu/~pasi/PTs/MRA_data/ (Cordonnier et al., 2025b). The complete MRA statistics per meteor shower, from which Table 1 was derived, are available at https://lda10g.alliance.unm.edu/~pasi/PTs/MRA_data/meteor_shower_table.csv. GMN meteor data are released under the CC BY 4.0 license, and can be accessed at https://globalmeteornetwork.org/data/ (Vida et al., 2019, 2021). The Orville archival radio data was downloaded from https://lda10g.alliance.unm.edu/Orville/ and processed using the Python scripts provided by the LWA collaboration at https://github.com/lwa-project/orville_wideband_imager (Dowell et al., 2020).

Meteor data were manipulated, organized, and saved using pandas v2.1.1 (https://pandas.pydata.org/; McKinney, 2010; The pandas Development Team, 2023). All figures displayed in this work were produced using matplotlib v3.8.0 (https://matplotlib.org/; Hunter, 2007). Sky coordinates and WCS implementation were handled with Astropy v5.3.4 (https://www.astropy.org/; Astropy Collaboration et al., 2022), with PyMap3d v3.0.1 being used to convert between geodetic and altitude/azimuth coordinates (https://pypi.org/project/pymap3d/; Hirsch, 2018). The gradient boosting classification algorithm was implemented using scikit-learn v1.3.1 (https://scikit-learn.org/; Pedregosa et al., 2011). The MSIS 2.1 atmospheric model used in calculating the K_B parameter was obtained via pymsis v0.8.0, a Python wrapper for the original Fortran source code (https://pypi.org/project/pymsis/; Emmert et al., 2022; Lucas, 2023). Background subtraction for the all-sky radio images made use of Photutils v1.11.0, an Astropy package for detection and photometry of astronomical sources (https://photutils.readthedocs.io/en/stable/; Bradley et al., 2024). Statistical tests, interpolations, and fit optimizations were performed using SciPy v1.8.0 (https://scipy.org/; Virtanen et al., 2020).

Acknowledgments

The authors thank Ralph Kelly and Jack Hines of Space Dynamics Laboratory for the design and construction of the WiPT2 system which was used to obtain all the PT data. The authors recognize and thank the multitude of GMN station operators whose time and effort enabled the meteor observations used in this work. Construction of the LWA has been supported by the Office of Naval Research under Contract N00014-07-C-0147. Support for operations and continuing development of the LWA is provided by the Air Force Research Laboratory (AFRL) and the National Science Foundation (NSF) under grant AST-2107845. L.E. Cordonnier and G.B. Taylor acknowledge support for this research from the NSF under Grant AST-1835400 and from AFRL. L.E. Cordonnier acknowledges support from an appointment to the AFRL Scholars Program at Kirtland Air Force Base, administered by Universities Space Research Association (USRA) through a contract with AFRL. This research was sponsored in part by the Air Force Office of Scientific Research (AFOSR) Lab Task 23RVCOR002. It was also funded in part by the NASA Space Weather Science Applications Operations 2 Research program, under Grant 20-SWO2R20_2-0007. D. Vida was supported in part by the NASA Meteoroid Environment Office under cooperative agreement 80NSSC21M0073. The views expressed are those of the authors and do not reflect the official guidance or position of the United States Government, the Department of Defense or of the United States Air Force. The appearance of external hyperlinks does not constitute endorsement by the United States Department of Defense (DoD) of the linked websites, or the information, products, or services contained therein. The DoD does not exercise any editorial, security, or other control over the information you may find at these locations.

References

Abe, S., Ebizuka, N., Murayama, H., Ohtsuka, K., Sugimoto, S., Yamamoto, M.-Y., et al. (2004). Video and photographic spectroscopy of 1998 and 2001 Leonid persistent trains from 300 to 930 nm. *Earth, Moon, and Planets*, *95*(1–4), 265–277. https://doi.org/10.1007/s11038-005-9031-0

Anderson, M. M., Hallinan, G., Eastwood, M. W., Monroe, R. M., Callister, T. A., Dowell, J., et al. (2019). New limits on the low-frequency radio transient sky using 31 hr of all-sky data with the OVRO–LWA. *The Astrophysical Journal*, *886*(2), 123. https://doi.org/10.3847/1538-4357/ab4f87

Astropy Collaboration, Price-Whelan, A. M., Lim, P. L., Earl, N., Starkman, N., Bradley, L., et al. (2022). The Astropy Project: Sustaining and growing a community-oriented open-source project and the latest major release (v5.0) of the core package. *The Astrophysical Journal*, *935*(2), 167. https://doi.org/10.3847/1538-4357/ac7c74

Baars, J. W. M., Genzel, R., Pauliny-Toth, I. I. K., & Witzel, A. (1977). The absolute spectrum of Cas A: An accurate flux density scale and a set of secondary calibrators. *Astronomy & Astrophysics*, *61*, 99–106.

Baggaley, W. J. (1976). The role of the oxides in meteoric species as a source of meteor train luminosity. *Monthly Notices of the Royal Astronomical Society*, *174*(3), 617–620. https://doi.org/10.1093/mnras/174.3.617

Beech, M. (1987). On the trail of meteor trains. *The Quarterly Journal of the Royal Astronomical Society*, *28*, 445.

Borovička, J. (2006). Meteor trains—Terminology and physical interpretation. *Journal of the Royal Astronomical Society of Canada*, *100*, 194.

Borovička, J., & Koten, P. (2003). Three phases in the evolution of Leonid meteor trains. In H. Yano, S. Abe, & M. Yoshikawa (Eds.), *ISAS Report SP: Proceedings of the 2002 International Science Symposium on the Leonid Meteor Storms* (Vol. 15, pp. 165–173). Institute of Space and Astronautical Science.

Bradley, L., Sipőcz, B., Robitaille, T., Tollerud, E., Vinícius, Z., Deil, C., et al. (2024). astropy/photutils: 1.11.0 [Software]. *Zenodo*. https://doi.org/10.5281/zenodo.10671725

Cairns, I. H. (1988). A semiquantitative theory for the 2f p radiation observed upstream from the Earth's bow shock. *Journal of Geophysical Research*, *93*(A5), 3958–3968. https://doi.org/10.1029/JA093iA05p03958

Calabretta, M. R., & Greisen, E. W. (2002). Representations of celestial coordinates in FITS. *Astronomy & Astrophysics*, *395*(3), 1077–1122. https://doi.org/10.1051/0004-6361:20021327

Ceplecha, Z. (1958). On the composition of meteors. *Bulletin of the Astronomical Institutes of Czechoslovakia*, *9*, 154.

Ceplecha, Z. (1988). Earth's influx of different populations of sporadic meteoroids from photographic and television data. *Bulletin of the Astronomical Institutes of Czechoslovakia*, *39*, 221.

Chau, J. L., Strelnikova, I., Schult, C., Oppenheim, M. M., Kelley, M. C., Stober, G., & Singer, W. (2014). Nonspecular meteor trails from non-field-aligned irregularities: Can they be explained by presence of charged meteor dust? *Geophysical Research Letters*, *41*(10), 3336–3343. https://doi.org/10.1002/2014GL059922

Clemesha, B. R., de Medeiros, A. F., Gobbi, D., Takahashi, H., Batista, P. P., & Taylor, M. J. (2001). Multiple wavelength optical observations of a long-lived meteor trail. *Geophysical Research Letters*, *28*(14), 2779–2782. https://doi.org/10.1029/2000GL012605

Cordonnier, L. E., Obenberger, K. S., Holmes, J. M., & Taylor, G. B. (2023). Persistent train and associated meteor data [Dataset]. *LWA Data Archive*. Retrieved from https://lda10g.alliance.unm.edu/~pasi/PTs/PT_tables/

Cordonnier, L. E., Obenberger, K. S., Holmes, J. M., Taylor, G. B., & Vida, D. (2024). Not so fast: A new catalog of meteor persistent trains. *Journal of Geophysical Research: Space Physics*, *129*(7), e2024JA032643. https://doi.org/10.1029/2024JA032643

Cordonnier, L. E., Obenberger, K. S., Holmes, J. M., Taylor, G. B., & Vida, D. (2025a). Connections between meteor persistent trains and ozone content in the mesopause region. *Earth and Space Science*, *12*(3), e2024EA003704. https://doi.org/10.1029/2024EA003704

Cordonnier, L. E., Obenberger, K. S., Holmes, J. M., Taylor, G. B., & Vida, D. (2025b). Meteor radio afterglow, persistent train, and associated meteor data [Dataset]. *LWA Data Archive*. Retrieved from https://lda10g.alliance.unm.edu/~pasi/PTs/MRA_data/meteor_data.csv

Cranmer, M. D., Barsdell, B. R., Price, D. C., Dowell, J., Garsden, H., Dike, V., et al. (2017). Bifrost: A Python/C++ framework for high-throughput stream processing in astronomy. *Journal of Astronomical Instrumentation*, *6*(4), 1750007. https://doi.org/10.1142/S2251171717500076

Dijkema, T., Bassa, C., Kuiack, M., Jenniskens, P., Johannink, C., Bettonvil, F., et al. (2021). Simultaneous broadband radio and optical emission of meteor trains imaged by LOFAR/AARTFAAC and CAMS. *WGN, Journal of the International Meteor Organization*, *49*(5), 137–141.

Dowell, J., Varghese, S., & Taylor, G. B. (2020). *The Orville wideband imager [Memo]*. LWA Memo Series. Retrieved from https://leo.phys.unm.edu/~lwa/memos/memo/lwa0215.pdf

Dyrud, L. P., Urbina, J., Fentzke, J. T., Hibbit, E., & Hinrichs, J. (2011). Global variation of meteor trail plasma turbulence. *Annales Geophysicae*, *29*(12), 2277–2286. https://doi.org/10.5194/angeo-29-2277-2011

Ellingson, S. W., Taylor, G. B., Craig, J., Hartman, J., Dowell, J., Wolfe, C. N., et al. (2013). The LWA1 radio telescope. *IEEE Transactions on Antennas and Propagation*, *61*(5), 2540–2549. https://doi.org/10.1109/TAP.2013.2242826

Emmert, J. T., Jones, M., Jr., Siskind, D. E., Drob, D. P., Picone, J. M., Stevens, M. H., et al. (2022). NRLMSIS 2.1: An empirical model of nitric oxide incorporated into MSIS. *Journal of Geophysical Research: Space Physics*, *127*(10), e2022JA030896. https://doi.org/10.1029/2022JA030896

Epstein, Z. B., Li, Y., Todorovski, D., & Hafizi, B. (2025). Theoretical estimation of passive HF signal from a meteorite plasma trail. In *2025 United States National Committee of URSI National Radio Science Meeting (USNC-URSI NRSM)* (pp. 157–158). https://doi.org/10.23919/USNC-URSINRSM66067.2025.10907201

Friedman, J. H. (2001). Greedy function approximation: A gradient boosting machine. *Annals of Statistics*, *29*(5), 1189–1232. https://doi.org/10.1214/aos/1013203451

Hapgood, M. A. (1980). IR observation of a persistent meteor train. *Nature*, *286*(5773), 582–583. https://doi.org/10.1038/286582a0

Higa, Y., Yamamoto, M.-Y., Toda, M., Maeda, K., & Watanabe, J.-I. (2005). Catalogue of persistent trains II: Images of Leonid meteor trains during the METRO campaign 1998-2002. *Publications of the National Astronomical Observatory of Japan*, *7*(4), 67–131.

Hirsch, M. (2018). PyMap3D: 3-D coordinate conversions for terrestrial and geospace environments. *Journal of Open Source Software*, *3*(23), 580. https://doi.org/10.21105/joss.00580

Hunter, J. D. (2007). Matplotlib: A 2D graphics environment. *Computing in Science & Engineering*, *9*(3), 90–95. https://doi.org/10.1109/MCSE.2007.55

Jenniskens, P., & Butow, S. J. (1999). The 1998 Leonid multi-instrument aircraft campaign—An early review. *Meteoritics & Planetary Sciences*, *34*(6), 933–943. https://doi.org/10.1111/j.1945-5100.1999.tb01411.x

Jenniskens, P., Lacey, M., Allan, B., Self, D., & Plane, J. (1998). FeO "orange arc" emission detected in optical spectrum of Leonid persistent train. *Earth, Moon, and Planets*, *82–83*, 429–438. https://doi.org/10.1023/A:1017079725808

Jewitt, D., Hsieh, H., & Agarwal, J. (2015). The active asteroids. In P. Michel, F. E. DeMeo, & W. F. Bottke (Eds.), *Asteroids IV* (pp. 221–241). University of Arizona Press. https://doi.org/10.2458/azu_uapress_9780816532131-ch012

Kelley, M. C. (2004). A new explanation for long-duration meteor radar echoes: Persistent charged dust trains. *Radio Science*, *39*(2). https://doi.org/10.1029/2003RS002988

Kelley, M. C., Gardner, C., Drummond, J., Armstrong, T., Liu, A., Chu, X., et al. (2000). First observations of long-lived meteor trains with resonance lidar and other optical instruments. *Geophysical Research Letters*, *27*(13), 1811–1814. https://doi.org/10.1029/1999GL011175

Kelley, M. C., Williamson, C. H. K., & Vlasov, M. N. (2013). Double laminar and turbulent meteor trails observed in space and simulated in the laboratory. *Journal of Geophysical Research: Space Physics*, *118*(6), 3622–3625. https://doi.org/10.1002/jgra.50339

Kruschwitz, C. A., Kelley, M. C., Gardner, C. S., Swenson, G., Liu, A. Z., Chu, X., et al. (2001). Observations of persistent Leonid meteor trails: 2. Photometry and numerical modeling. *Journal of Geophysical Research*, *106*(A10), 21525–21541. https://doi.org/10.1029/2000JA000174

Lane, W. M., Cotton, W. D., Helmboldt, J. F., & Kassim, N. E. (2012). VLSS redux: Software improvements applied to the very large array low-frequency sky survey. *Radio Science*, *47*(6). https://doi.org/10.1029/2011RS004941

Lane, W. M., Cotton, W. D., van Velzen, S., Clarke, T. E., Kassim, N. E., Helmboldt, J. F., et al. (2014). The very large array low-frequency sky survey redux (VLSSr). *Monthly Notices of the Royal Astronomical Society*, *440*(1), 327–338. https://doi.org/10.1093/mnras/stu256

Lei, J., & Dagdigian, P. J. (2000). Identification of new bands in the orange system of FeO. *Journal of Molecular Spectroscopy*, *203*(2), 345–348. https://doi.org/10.1006/jmsp.2000.8195

Lucas, G. (2023). pymsis [Software]. *Zenodo*. https://doi.org/10.5281/zenodo.8403883

Malaspina, D. M., Cairns, I. H., & Ergun, R. E. (2012). Antenna radiation near the local plasma frequency by Langmuir wave eigenmodes. *The Astrophysical Journal*, *755*(1), 45. https://doi.org/10.1088/0004-637X/755/1/45

Mathews, J. D., & Djuth, F. T. (2017). Meteoroid flaring as a possible source of intense Langmuir waves. In *2017 XXXIInd General Assembly and Scientific Symposium of the International Union of Radio Science (URSI GASS)* (pp. 1–4). https://doi.org/10.23919/URSIGASS.2017.8105190

McKinney, W. (2010). Data structures for statistical computing in Python. In S. van der Walt & J. Millman (Eds.), *Proceedings of the 9th Python in Science Conference* (pp. 56–61). https://doi.org/10.25080/Majora-92bf1922-00a

Obenberger, K. S., Dowell, J. D., Hancock, P. J., Holmes, J. M., Pedersen, T. R., Schinzel, F. K., & Taylor, G. B. (2016). Rates, flux densities, and spectral indices of meteor radio afterglows. *Journal of Geophysical Research: Space Physics*, *121*(7), 6808–6817. https://doi.org/10.1002/2016JA022606

Obenberger, K. S., Holmes, J. M., Ard, S. G., Dowell, J., Shuman, N. S., Taylor, G. B., et al. (2020). Association between meteor radio afterglows and optical persistent trains. *Journal of Geophysical Research: Space Physics*, *125*(9), e2020JA028053. https://doi.org/10.1029/2020JA028053

Obenberger, K. S., Holmes, J. M., Dowell, J. D., Schinzel, F. K., Stovall, K., Sutton, E. K., & Taylor, G. B. (2016). Altitudinal dependence of meteor radio afterglows measured via optical counterparts. *Geophysical Research Letters*, *43*(17), 8885–8892. https://doi.org/10.1002/2016GL070059

Obenberger, K. S., Taylor, G. B., Hartman, J. M., Dowell, J., Ellingson, S. W., Helmboldt, J. F., et al. (2014). Detection of radio emission from fireballs. *The Astrophysical Journal Letters*, *788*(2), L26. https://doi.org/10.1088/2041-8205/788/2/L26

Obenberger, K. S., Taylor, G. B., Lin, C. S., Dowell, J., Schinzel, F. K., & Stovall, K. (2015). Dynamic radio spectra from two fireballs. *Journal of Geophysical Research: Space Physics*, *120*(11), 9916–9928. https://doi.org/10.1002/2015JA021229

Oppenheim, M. M., & Dimant, Y. S. (2016). Photoelectron-induced waves: A likely source of 150 km radar echoes and enhanced electron modes. *Geophysical Research Letters*, *43*(8), 3637–3644. https://doi.org/10.1002/2016GL068179

Pedregosa, F., Varoquaux, G., Gramfort, A., Michel, V., Thirion, B., Grisel, O., et al. (2011). Scikit-learn: Machine learning in Python. *Journal of Machine Learning Research*, *12*, 2825–2830.

Platonov, K. Y., & Fleishman, G. D. (2002). Transition radiation in media with random inhomogeneities. *Physics-Uspekhi*, *45*(3), 235–291. https://doi.org/10.1070/pu2002v045n03abeh000952

Popov, A. M., Berezhnoy, A. A., Borovička, J., Labutin, T. A., Zaytsev, S. M., & Stolyarov, A. V. (2020). Tackling the FeO orange band puzzle in meteor and airglow spectra through combined astronomical and laboratory studies. *Monthly Notices of the Royal Astronomical Society*, *500*(4), 4296–4306. https://doi.org/10.1093/mnras/staa3487

Russell, R. W., Rossano, G. S., Chatelain, M. A., Lynch, D. K., Tessensohn, T. K., Abendroth, E., et al. (1998). Mid-infrared spectroscopy of persistent Leonid trains. *Earth, Moon, and Planets*, *82*, 439–456. https://doi.org/10.1023/A:1017083811695

Schleyer, F., Cairns, I. H., & Kim, E.-H. (2014). Linear mode conversion of Langmuir/z mode waves to radiation: Averaged energy conversion efficiencies, polarization, and applications to Earth's continuum radiation. *Journal of Geophysical Research: Space Physics*, *119*(5), 3392–3410. https://doi.org/10.1002/2013JA019364

Smith, A. K., Harvey, V. L., Mlynczak, M. G., Funke, B., García-Comas, M., Hervig, M., et al. (2013). Satellite observations of ozone in the upper mesosphere. *Journal of Geophysical Research: Atmospheres*, *118*(11), 5803–5821. https://doi.org/10.1002/jgrd.50445

The pandas Development Team. (2023). pandas-dev/pandas: Pandas [Software]. *Zenodo*. https://doi.org/10.5281/zenodo.8092754

Tingay, S. J., Goeke, R., Bowman, J. D., Emrich, D., Ord, S. M., Mitchell, D. A., et al. (2013). *The Murchison widefield array: The square kilometre array precursor at low radio frequencies* (Vol. 30, p. e007). Publications of the Astronomical Society of Australia. https://doi.org/10.1017/pasa.2012.007

Trowbridge, C. C. (1907). Physical nature of meteor trains. *The Astrophysical Journal*, *26*(2), 191–205. https://doi.org/10.1086/141478

Ulm, K. (1990). A simple method to calculate the confidence interval of a standardized mortality ratio (SMR). *American Journal of Epidemiology*, *131*(2), 373–375. https://doi.org/10.1093/oxfordjournals.aje.a115507

van Haarlem, M. P., Wise, M. W., Gunst, A. W., Heald, G., McKean, J. P., Hessels, J. W. T., et al. (2013). LOFAR: The LOw-Frequency ARray. *Astronomy & Astrophysics*, *556*, A2. https://doi.org/10.1051/0004-6361/201220873

Varghese, S. S., Dowell, J., Obenberger, K. S., Taylor, G. B., Anderson, M., & Hallinan, G. (2024). Spatially resolved observations of meteor radio afterglows with the OVRO-LWA. *Journal of Geophysical Research: Space Physics*, *129*(2), e2023JA032272. https://doi.org/10.1029/2023JA032272

Varghese, S. S., Dowell, J., Obenberger, K. S., Taylor, G. B., & Malins, J. (2021). Broadband imaging to study the spectral distribution of meteor radio afterglows. *Journal of Geophysical Research: Space Physics*, *126*(10), e2021JA029296. https://doi.org/10.1029/2021JA029296

Varghese, S. S., Obenberger, K. S., Taylor, G. B., & Dowell, J. (2019). Testing the radiation pattern of meteor radio afterglow. *Journal of Geophysical Research: Space Physics*, *124*(12), 10749–10759. https://doi.org/10.1029/2019JA026922

Vasilyev, R. V., Syrenova, T. E., Beletsky, A. B., Artamonov, M. F., Merzlyakov, E. G., Podlesny, A. V., & Cedric, M. V. (2021). Studying a long-lasting meteor trail from stereo images and radar data. *Atmosphere*, *12*(7), 841. https://doi.org/10.3390/atmos12070841

Vida, D., Brown, P. G., Devillepoix, H. A. R., Wiegert, P., Moser, D. E., Matlovič, P., et al. (2023). Direct measurement of decimetre-sized rocky material in the Oort cloud. *Nature Astronomy*, *7*(3), 318–329. https://doi.org/10.1038/s41550-022-01844-3

Vida, D., Gural, P. S., Brown, P. G., Campbell-Brown, M., & Wiegert, P. (2019). Estimating trajectories of meteors: An observational Monte Carlo approach—I. Theory. *Monthly Notices of the Royal Astronomical Society*, *491*(2), 2688–2705. https://doi.org/10.1093/mnras/stz3160

Vida, D., Šegon, D., Gural, P. S., Brown, P. G., McIntyre, M. J. M., Dijkema, T. J., et al. (2021). The global meteor network—Methodology and first results. *Monthly Notices of the Royal Astronomical Society*, *506*(4), 5046–5074. https://doi.org/10.1093/mnras/stab2008

Virtanen, P., Gommers, R., Oliphant, T. E., Haberland, M., Reddy, T., Cournapeau, D., et al. (2020). SciPy 1.0: Fundamental algorithms for scientific computing in Python. *Nature Methods*, *17*(3), 261–272. https://doi.org/10.1038/s41592-019-0686-2

West, J. B., & Broida, H. P. (1975). Chemiluminescence and photoluminescence of diatomic iron oxide. *The Journal of Chemical Physics*, *62*(7), 2566–2574. https://doi.org/10.1063/1.430837

Whipple, F. L. (1955). The physical theory of meteors. VII. On meteor luminosity and ionization. *The Astrophysical Journal*, *121*, 241–249. https://doi.org/10.1086/145981

Yamamoto, M.-Y., Toda, M., Higa, Y., Maeda, K., & Watanabe, J.-I. (2004). Altitudinal distribution of 20 persistent meteor trains: Estimates derived from metro campaign archives. *Earth, Moon, and Planets*, *95*(1–4), 279–287. https://doi.org/10.1007/s11038-005-9048-4

Zhang, X., Hancock, P., Devillepoix, H. A. R., Wayth, R. B., Beardsley, A., Crosse, B., et al. (2018). Limits on radio emission from meteors using the MWA. *Monthly Notices of the Royal Astronomical Society*, *477*(4), 5167–5176. https://doi.org/10.1093/mnras/sty930

Zhao, F., Liang, R., Yang, Z., Shan, H., Zheng, Q., Zhang, Q., & Guo, Q. (2023). The intensity of diffuse galactic emission reflected by meteor trails. *Monthly Notices of the Royal Astronomical Society*, *527*(2), 4140–4152. https://doi.org/10.1093/mnras/stad3429

Zhu, C., Byrd, R. H., Lu, P., & Nocedal, J. (1997). Algorithm 778: L-BFGS-B: Fortran subroutines for large-scale bound-constrained optimization. *ACM Transactions on Mathematical Software*, *23*(4), 550–560. https://doi.org/10.1145/279232.279236

Zinn, J., & Drummond, J. (2005). Observations of persistent Leonid meteor trails: 4. Buoyant rise/vortex formation as mechanism for creation of parallel meteor train pairs. *Journal of Geophysical Research*, *110*(A4), A04306. https://doi.org/10.1029/2004JA010575